A Constraint Correction Method Based on Use of a Single Test Specimen

M. Gintalas[a,*], R.A. Ainsworth[b]

[a] *Brunel University London, Department of Mechanical and Aerospace Engineering, NSIRC, Cambridge, CB21 6AL, UK*
[b] *The University of Manchester, School of Mechanical, Aerospace and Civil Engineering, Pariser Building, Sackville Street, Manchester M13 9PL, UK*

Abstract

Commonly, fracture toughness tests on deeply cracked specimens are used to assess defects in large-scale components. The paper presents a method for selection of test specimen type, size and crack length in order to obtain fracture toughness estimates relevant to defects in cracked pipes. The method uses available closed-form T-stress, stress intensity factor and limit load solutions to determine the required specimen dimensions. The paper reports elastic-plastic finite element analyses for single edge notched bend (SENB) and single edge notched tension (SENT) specimens and cracked pipes which demonstrate good agreement of the matching approach, although care is needed in selecting the appropriate limit load solution for SENT geometries.

Keywords: constraint, fracture toughness, component assessment

---

[*] Corresponding author. Email address: marius.gintalas@brunel.ac.uk

Nomenclature

a	crack depth of SENB, SENT and CT specimen or FCC pipe
B	SENB or SENT specimen thickness
E	Young's modulus
H	specimen or pipe length
J	J-integral
M	pure bending moment
m	Load parameter
n	parameter for R-O material
P	applied load
Q	elastic-plastic constraint parameter
T	T-stress
t	wall thickness of TWC pipe
W	height of SENB, SENT and CT specimen or wall thickness of FCC pipe
α	relative crack depth
β_{T}	normalised constraint parameter
ϵ	elastic-plastic strain
ϵ_0	strain at σ_{y}
φ	angular position at the crack tip
μ	parameter for R-O material
ν	Poisson's ratio
ϕ	plastic zone size parameter
σ_{y}	yield strength

θ	half crack angle in TWC pipe
A_2	elastic-plastic constraint parameter
a_e	effective crack length
E'	plain strain Young's modulus
f_α	non-dimensional stress intensity factor function
f_L	non-dimensional limit load function
h_1	parameter for J_{pl}
J_{el}	elastic J-integral
J_{pl}	elastic-plastic J-integral
K_I	stress intensity factor for fracture mode-I
L_r	ratio of applied load to limit load
M_L	limit bending moment
P_L	limit load
R_e	external radius
R_i	internal radius
R_m	mean radius
r_y	plastic zone size
T_z	out-of-plane constraint parameter
2D	two-dimensional
3D	three-dimensional
CT	compact tension specimen
CTOD-R	crack tip opening displacement resistance curve
EPH	elastic-plastic with hardening material

EPP	elastic perfectly plastic material
FAD	failure assessment diagram
FCC	pipe with fully circumferential internal crack
FEA	finite element analysis
J-R	crack growth resistance curve
LLB	leak before break
MPC	multi-point constraint
R-O	Ramberg-Osgood material
SENB	single edge notched bend specimen
SENB-c	corrected SENB specimen size
SENT	single edge notched tension specimen
SENT(C)	single edge notched clamped tensile specimen
SENT(C)-c	corrected SENT(C) specimen size
SENT(P)	single edge notched pin-loaded tensile specimen
SENT(P)-c	corrected SENT(P) specimen size
SSY	small-scale yielding
TWC	circumferentially through-wall cracked pipe

1. Introduction

SENB or compact tension (CT) specimens with deep cracks (a/W =0.5, where a is the crack length and W is the specimen height) are usually used to measure fracture toughness of steels. These specimens represent high constraint at the crack tip and are used in standard fracture toughness determination methods [1]. Surface defects such as corrosion cracks, welding cracks, defects formed in the manufacturing process and in service of pressure pipelines and vessels often have lower crack-tip constraint. The use of fracture toughness obtained from deeply cracked specimens with high constraint in a design or a life assessment of pipes is then conservative [2]. Therefore, results obtained from high constraint specimen configurations cannot be directly transferred to provide an accurate assessment of a low constraint condition, for example, a pressurised pipeline experiencing longitudinal strains [3]. Not only crack initiation, but also crack growth toughness depends on constraint. This highlights the importance and relevance of constraint in fracture mechanics field.

In leak before break (LBB) analysis, to obtain the crack growth (J-R) or crack tip opening displacement (CTOD) resistance curves, standard fracture toughness specimens, such as SENB specimens with deep cracks, are also used to ensure high crack-tip constraint. The constraint influences the ductile tearing resistance of the material and therefore the resulting J-R curves affect the predicted LBB behaviour [4]. For the same material, high constraint configurations yield relatively low resistance curves, while shallow SENB and predominantly tension loaded configurations develop a higher resistance to ductile tearing and larger toughness values at similar amounts of crack growth. Consequently, the issue of the transferability of experimentally measured fracture resistance data to structural piping components remains important for accurate predictions of LBB, in-service residual strength and remaining life [5, 6].

From an experimental point of view, the SENT specimen configuration has been shown to provide a more representative crack tip constraint and a better characterization of the resistance curve behaviour than SENB or CT specimens for low constraint conditions [3, 7, 8]. It has been found that the crack-tip constraint of the SENT specimen is similar to that of a full-scale pipe containing a surface crack under longitudinal tension or internal pressure [9, 10, 11]. More specifically, compared to the single edge notched tensile clamped (SENT(C)) specimen, the crack-tip constraint of a single edge notched tension pin-loaded (SENT(P)) specimen is closer to that of axially cracked pipes [2, 12]. Hence the use of resistance curves determined from SENT specimens can lead to more accurate assessments of pipelines containing cracks.

In [5], it was found that SENB and SENT samples in certain a/W regimes demonstrate similar crack tip constraint. Shallow cracked SENB specimens with crack sizes in the range of $0.1 \leq a/W \leq 0.2$ exhibit levels of crack-tip constraint similar to clamped SENT(C) specimens having crack sizes in the range $0.2 \leq a/W \leq 0.4$. Also, J-R curves for the SENB specimens depend rather strongly on crack size, particularly for $a/W \leq 0.3$. In contrast, J-R curves for clamped SENT(C) specimens display little sensitivity to a/W ratio. Shallow cracked SENB specimens with crack sizes in the range $0.1 \leq a/W \leq 0.2$ provide fracture response in terms of J-R curves in good agreement with the corresponding fracture behaviour of circumferentially cracked pipes.

Tests on specimens with shallow, edge cracks provide elevated values of fracture toughness measured by the J-integral when compared with those obtained from standard deeply cracked high constraint specimens. This increase in toughness occurs because shallow-edge cracked geometries impose a relatively low level of crack-tip constraint [13]. A single fracture mechanics parameter, stress intensity factor or J-integral, cannot explain constraint and the variation in fracture toughness due to different constraint levels. The aim of some research has therefore been to find a second parameter that can characterise constraint, so that results from one test geometry can be transferred to another geometry [14]. There have been analytical, numerical and experimental studies to attempt to describe fracture in terms of the J-integral and a second parameter [15, 16]. The second parameter provides further information concerning how the structural and loading configuration affects the constraint conditions at the crack-tip.

Two-parameter approaches, K-T, J-Q and J-A_2, have been developed to address the constraint effect [17]. The K-T approach is based on the elastic asymptotic expansion where T-stress is proportional to the applied load. However, the higher order terms in the elastic-plastic material vary non-linearly with the applied load. These terms are taken into account by Q or A_2 parameters. There is a relationship between T-stress and the Q parameter. For power law materials it has been derived from plain strain modified boundary layer analysis and presented by a cubic polynomial [18]. For perfectly plastic materials the relationship is simplified to $Q = T/\sigma_y$, when $-0.5 < T/\sigma_y \leq 0$ and $Q = 0.5T/\sigma_y$, when $0 < T/\sigma_y < 0.5$ [18]. The two-parameter approaches, K-T, J-Q and J-A_2, were derived for two dimensional stress fields to address in-plane constraint. The stress distribution at the crack tip of a real crack is three dimensional and the stress state varies through the thickness of the specimen. The third parameter, which takes into account out-of-plane constraint, T_z, was added to already existing two-parameter methods. They became extended for three dimensional stress states in the form of $J - A_2 - T_z$ or J-Q-T_z [19, 20, 21, 22].

The T-stress is an elastic parameter which quantifies crack tip constraint. T-stress is the constant stress acting parallel to the crack flank in an elastic analysis [23]. Positive T-stress is characteristic of high constraint and negative T-stress of low constraint geometries. The T-stress affects the size of the plastic zone [24] and also influences the crack growth path [25]. For instance, crack path deviations up to 50° have been observed when testing low constraint shallow cracked SENT(C) samples [26]. Negative values of the T-stress serve to reduce crack-tip constraint and so increase measured fracture toughness [13].

In order to obtain representative fracture toughness data for structural components using laboratory specimens, the constraint levels in both specimen and component should be as similar as possible. Therefore, constraint corrections can be applied and these are described in R6 [27] and BS 7910 [28, 29]. The elastic constraint parameter, T-stress, is used for constraint correction when the applied load is less than or equal to the limit load. One of the difficulties with the constraint correction procedures described in R6 or BS 7910 is that a number of specimens with different crack lengths are generally required to generate a function describing the dependence of fracture toughness on constraint [28]. The function generated is then used to construct a constraint modified failure assessment diagram (FAD).

The work presented in this paper aims to develop further an alternative single specimen constraint correction method initially introduced in [30, 31]. The approach has the potential to reduce conservatism in both crack initiation and crack propagation toughness measurement procedures. The method has also been summarised in [32] where the main idea was highlighted and compared with the constraint correction procedure in R6. The method is based on three fracture parameters: stress intensity factor, T-stress and limit load. The approach allows the choice of specimen and crack size, which results in T-stress, stress intensity factor and amount of plastic work, being the same as for a cracked component. It is assumed that when both the T-stress and stress intensity factor elastic parameters of a specimen and a component are matched, the plastic J-integral should follow a similar path up to the limit load. Elastic-plastic finite element analyses are presented in this paper to assess this hypothesis.

2. Method

In this section the simplified constraint correction approach presented in [30, 31] is described qualitatively. Section 3 then presents the information required to apply the method for some particular geometries while later sections illustrate the results of applying the approach by comparison with finite element solutions for the geometries addressed in Section 3.

The approach requires that a normalised constraint parameter β_{T}, a limit load solution and a stress intensity factor solution are known for two geometries: the cracked component being assessed and the test specimen being used to generate the fracture toughness data. The method then consists of three steps.

In step 1, the normalised constraint parameter β_{T} for the two geometries has to be matched. It will be seen from the solutions presented in Section 3 that once a test specimen geometry has been selected (e.g. SENT), the parameter β_{T} only depends on a/W ratio and therefore this step involves selection of a/W in the test specimen. This step ensures that the two geometries although different in size and having different crack sizes experience the same constraint level (e.g. T-stress) for the same ratio of applied load to limit load. Thus, loading the two geometries up to their respective limit loads results in similar amount of plasticity and constraint.

Step 2 of the method is to choose an applied load equal to the limit load, which essentially results in the ratio of applied load to limit load, $\mathrm{L_r}$, being equal to 1.0. The parameter $\mathrm{L_r}$ is the measure of proximity to plastic collapse. Completion of steps 1 and 2 ensures the same level of constraint and the same amount of plasticity introduced in the two geometries. In principle, any load level can be chosen in step 2 provided that the values of $\mathrm{L_r}$ in the specimen and component are equal as this does not affect step 3.

In step 3, the stress intensity factor in the specimen is matched to that in the component by varying the specimen size (W) but keeping the ratio of applied load to limit load set in step 2 and also keeping the a/W ratio set in step 1.

3. Closed form stress intensity factor, T-stress and limit load solutions

To apply the method of Section 2, stress intensity factor for opening mode $\mathrm{K_I}$, T-stress and limit load solutions are required. The solution normalisations are summarised here for selected specimen and pipe geometries, with algebraic details of the solutions given in an Appendix. The specimen geometries include three-point SENB and SENT specimens. The pipe geometries include pipes with through-wall circumferential (TWC) and fully circumferential internal cracks (FCC). The solutions are taken from [27, 29, 33, 34]. The geometries considered are shown schematically in Figures 1-4.

In the Appendix, the stress intensity factor solutions are generally presented as a function of the relative crack depth, $\alpha = \mathrm{a/W}$ in terms of a non-dimensional function f_α while the limit load solutions are presented in terms of a non-dimensional function $\mathrm{f_L}$, evaluated using the von Mises yield criterion. The T-stress is presented in normalised form in terms of the parameter β_T defined by:

$$\beta_\mathrm{T} = \mathrm{T/L_r}\sigma_\mathrm{y} \tag{1}$$

where $\mathrm{L_r}$ is the ratio of applied load, P, to the limit load $\mathrm{P_L}$ defined for a perfectly plastic material with yield stress σ_y.

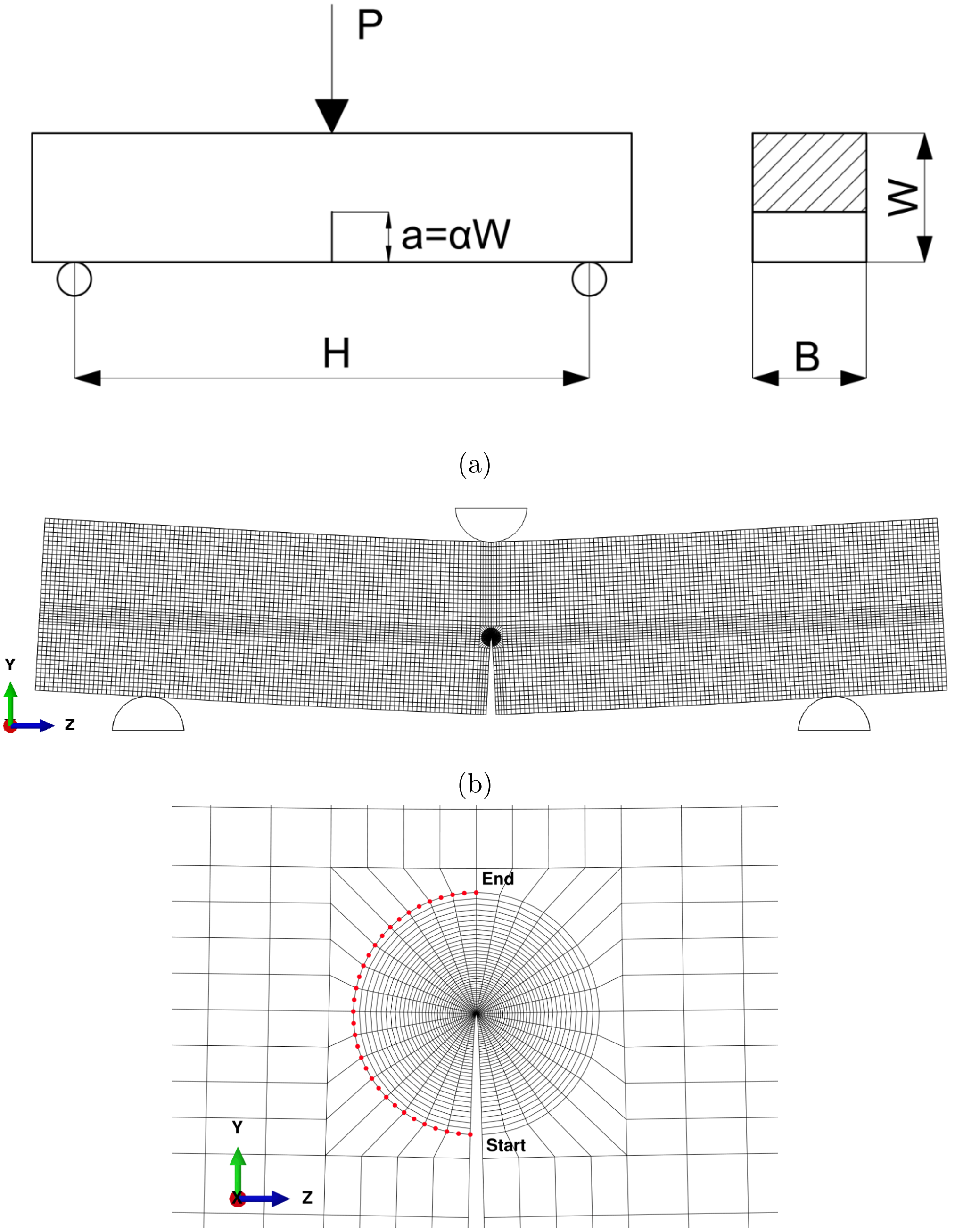

(a)

(b)

(c)

Figure 1: Three-point SENB specimen - SENB: (a) schematic drawing, (b) finite element model of SENB with $\alpha = 0.45$ (see also Table 1), (c) crack tip zone with highlighted path for strain extraction

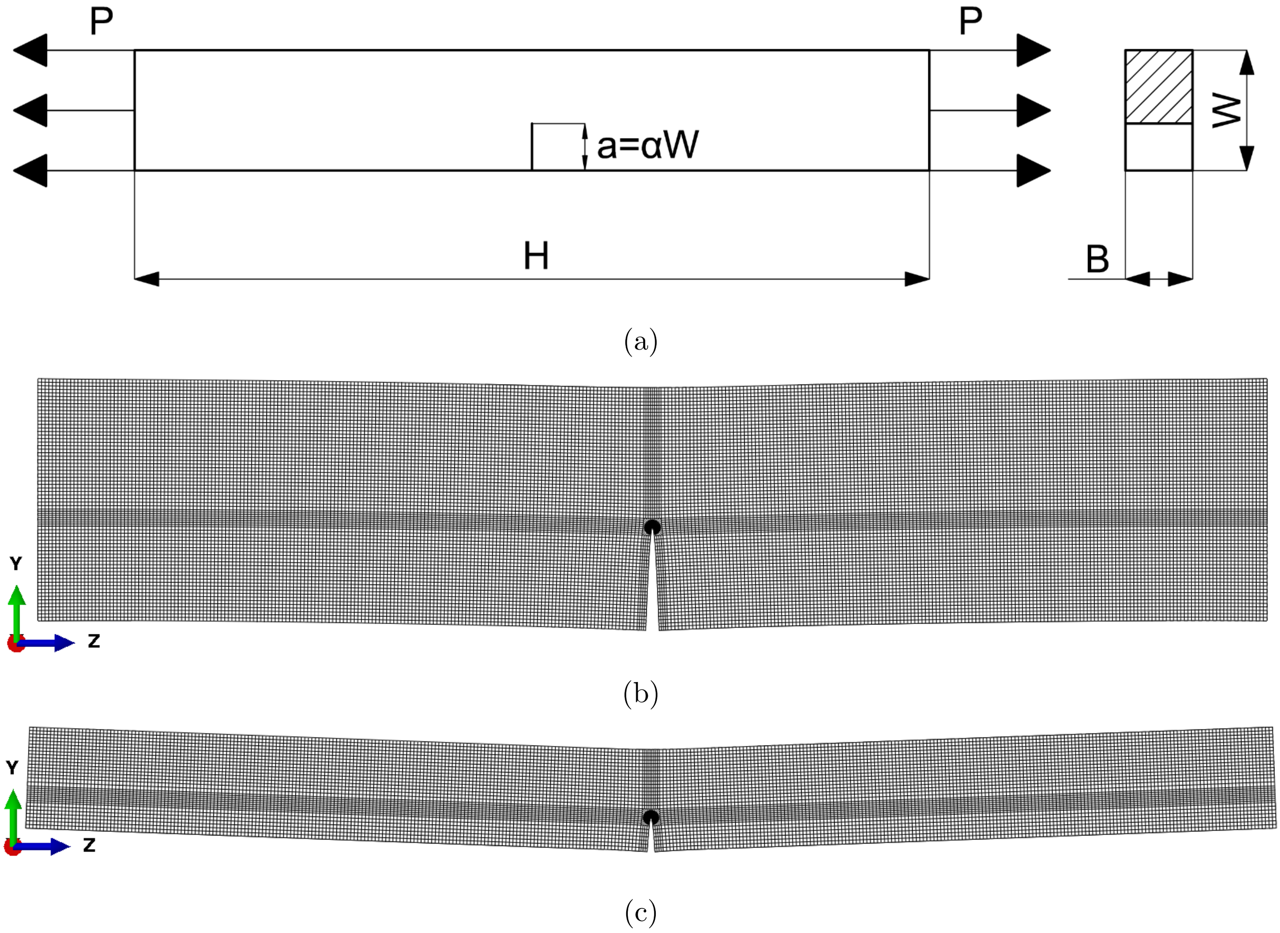

Figure 2: Single edge notched tension specimen (SENT): (a) schematic drawing, (b) Finite element model of SEN(C) for $\alpha = 0.426$ (see also Table 6), (c) Finite element model of SENT(P) for $\alpha = 0.336$ (see also Table 5)

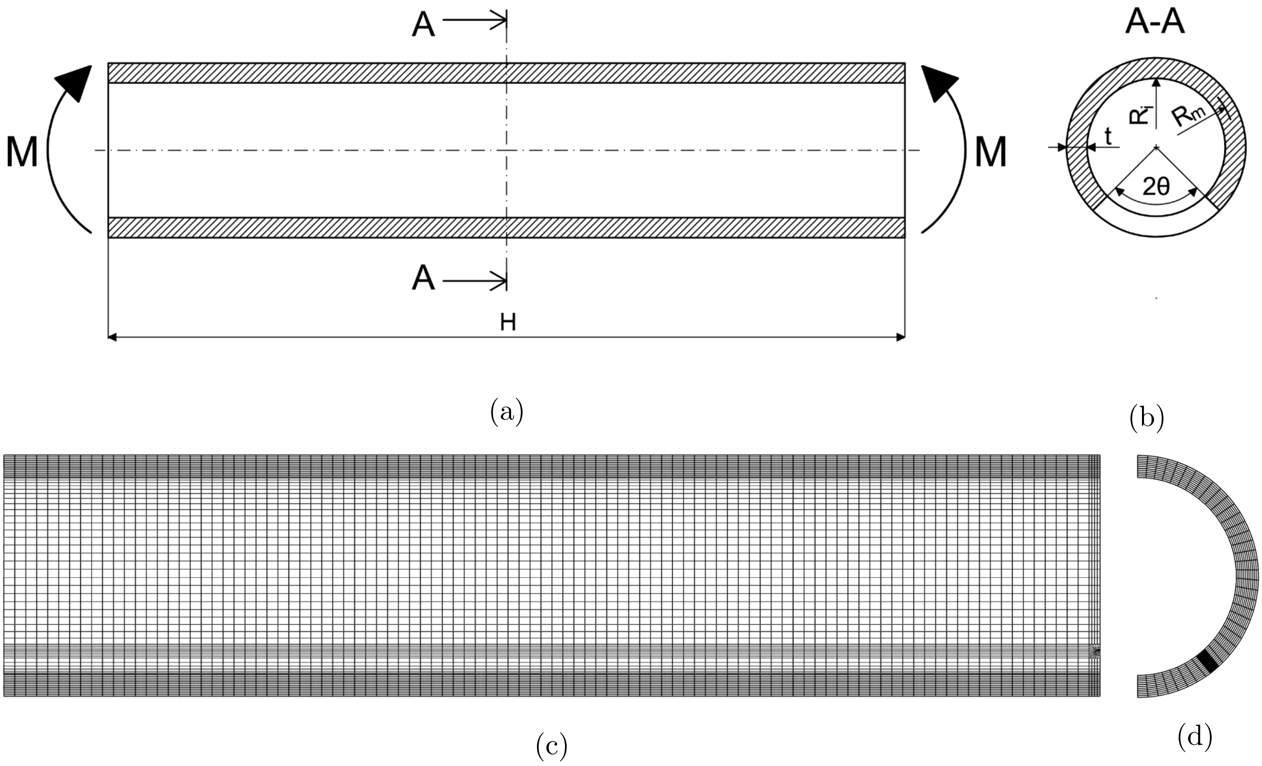

Figure 3: Circumferentially through wall cracked (TWC) pipe with $\alpha = 0.22$ (Table 6): (a) schematic view of pipe under pure bending moment, (b) pipe cross-section, (c) mesh view from inner surface, (d) mesh view from A-A direction

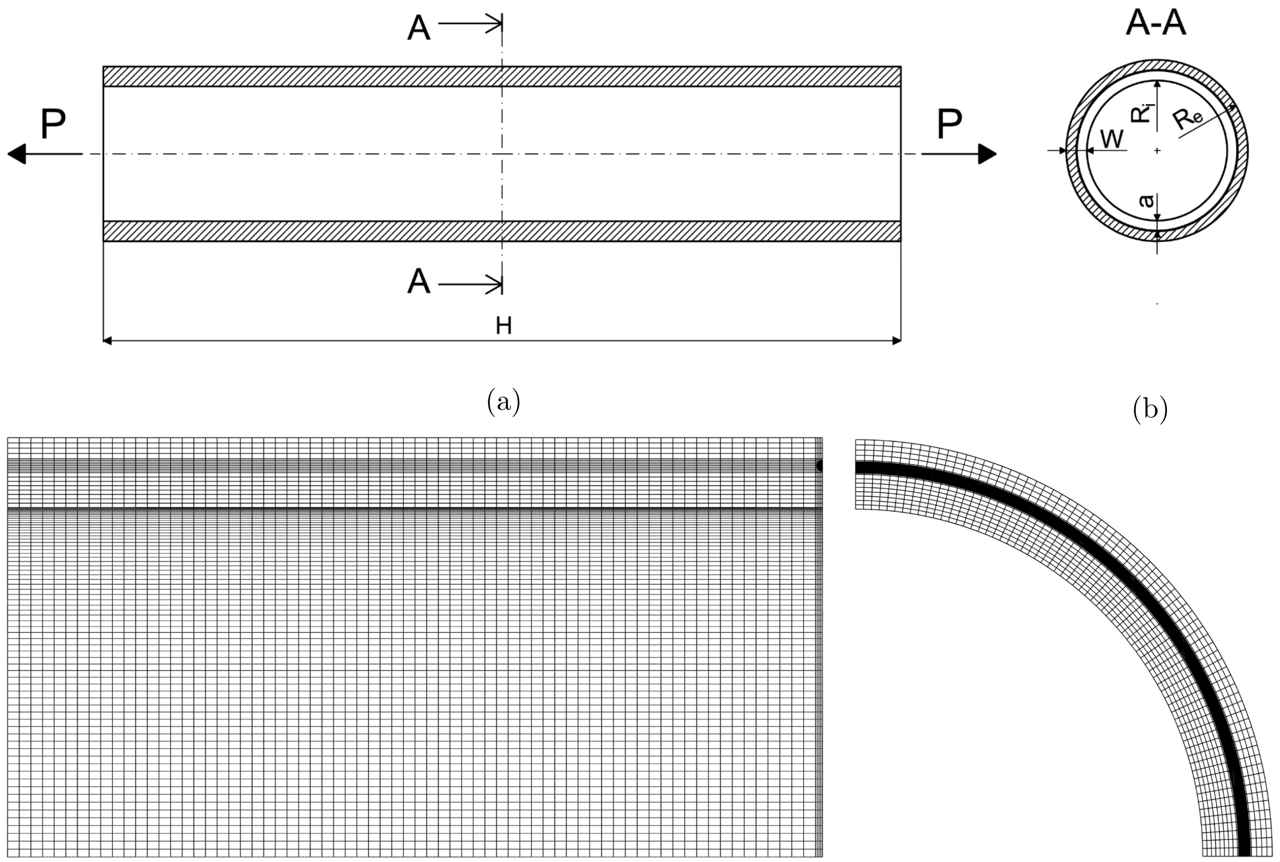

(a)

(b)

(c)

(d)

Figure 4: Pipe with fully circumferential internal crack (FCC) with alpha = 0.6 (Table 8): (a) schematic view of pipe subjected to tension load, (b) pipe cross-section, (c) finite element model of 1/4 pipe segment, (d) cross-section mesh view

4. Finite element models

ABAQUS 2018 was used to run the simulations. The finite element model of the SENB specimen is shown in Fig. 1b. Both support and load rollers were modelled as analytical surfaces including surface-to-surface type contact between them and the corresponding surfaces. No friction or damping was introduced in contact definition.

Clamping for the SENT(C) geometry (Fig. 2b) was implemented by creating a reference point in the middle of the cross section at the end of the specimen. Rigid constraint links were applied via the multi-point constraint (MPC) option in ABAQUS between the reference point and the end surface of the specimen. Rotation of the linked surface was restricted, therefore it remained perpendicular to the load vector. A concentrated force was then applied on the reference point. This type of constraint and loading results in uniform displacement of all nodes at the linked surface.

Pin-loading creates an uniform stress distribution along the W edge of the SENT specimen. This type of loading was simulated by applying a constant pressure directly at the end surfaces of the specimen. Rotation of the end surfaces was not restricted and therefore the end surfaces did not remain perpendicular to the load vector (Fig. 2c).

The bending moment on the through-wall circumferentially cracked pipe was applied via a reference point placed on the pipe axis at the end of the pipe. The reference point was connected with the pipe end surface using rigid constraint links via the MPC constraint option in ABAQUS. Two cuts through symmetry planes were applied to simplify the model (Fig. 3c and 3d).

For the pipe with a fully circumferential internal crack the axial load was applied via an equivalent pressure acting on the end surface of the pipe. Three cuts through symmetry planes were applied to simplify the model (Fig. 4c and 4d).

4.1. Elastic analysis

The finite element models were validated against available elastic solutions from the literature in terms of stress intensity factor and the β_{T} parameter. Results for stress intensity factor are summarised in Fig. 5a and those for β_{T} in Fig. 5b. All specimens were simulated in a three-dimensional state using C3D20 elements. Plane strain was implemented by applying boundary conditions on side surfaces of the sample suppressing lateral (out-of-plane) displacement (X-axis direction in Fig. 1b, Fig. 2b and 2c). One element per thickness was used in plane strain models. For three-dimensional cases, these boundary conditions were released and more elements added in thickness direction. It is apparent from Fig. 5 that very close agreement between reference solutions and FEA results is obtained in all cases.

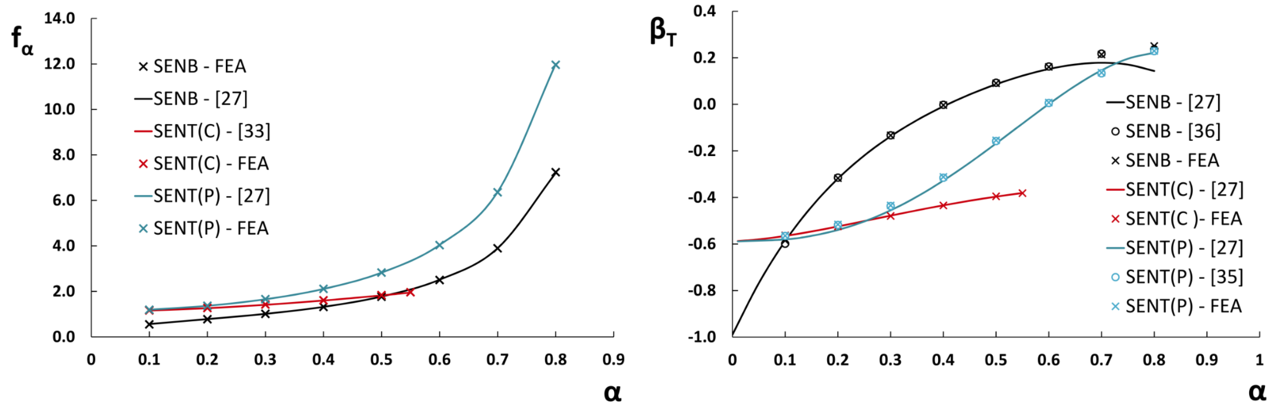

(a) (b)

Figure 5: Comparison of results from elastic finite element analyses with solutions from the literature [27, 33, 49, 50]: (a) normalised stress intensity factor, (b) normalised constraint parameter

4.2. Elastic-plastic analysis

The J-integral is path-independent when the material is non-linear elastic. As such, path-independence of J holds in elastic-plastic materials when the material response is governed by the deformation theory of plasticity or when flow theory mimics deformation theory such as when proportional loading occurs at all points within the domain [35]. In general, the deformation plasticity model is a non-linear elastic model with a limit state when all of a specimen or structure is responding plastically [36]. According to the deformation theory of plasticity the hydrostatic stress does not contribute to plastic strain [17]. The J-integral obtained with a deformation plasticity model exhibits contour independence (Fig. 6b). In any situation where a significant amount of non-proportional loading occurs, it is expected that the J-integral will not be path-independent.

The incremental plasticity option was chosen for elastic-plastic analysis in this work and therefore some non-proportional loading and path dependence of the J-integral may be expected. The path dependence of the incremental-theory calculations is sensitive to the presence of T-stresses [37]. Two material models with the incremental plasticity option were used in this work: elastic-plastic with hardening (EPH) and elastic perfectly plastic (EPP), Fig. 6a. The elastic-plastic J-integral values, J_{pl}, were output at 40 contours for each load increment to form a J_{pl} curve as a function of load. Fig 6b shows the typical J-integral path dependence resulting from use of the EPH material, where the minimum value is reached before the 40^{th} contour. For comparison, the J_{pl} curve for the same geometry and load level with a Ramberg-Osgood (R-O) material is shown. Other $J_{pl} - L_r$ curves in this work were constructed using the minimum value of J_{pl} except those in Fig. 7.

Within the incremental plasticity option, J_{pl} values might saturate relatively far away from the crack tip [38]. This could be an issue for shallow cracks. For example, the radius of the outermost contour where J_{pl} values would saturate might be greater than the crack depth. If the radius of the outermost contour is large enough, it might interact with the sample edge or the local strain field originating from an applied load or boundary conditions. Therefore, it was decided to work with the minimum value of J_{pl}. Based on minimum J_{pl}, both strain field and J_{pl} values can be matched in two geometries. The $J_{pl} - L_r$ curves of EPH material in Fig. 6a proves that the minimum value of J_{pl} is a reliable parameter for the strain matching purpose. The J_{pl} curves for EPH material are of the same trend and have a minimum value of J_{pl}. These curves represent different samples, SENB 0.1669, SENT(P) 0.294 and SENT(P) 0.4416 (Section 6.3 and 6.4), having very similar strain field at the crack tip (Fig. 13) and J_{pl} values (Table 4-5). On the other hand, for the matching exercise the absolute value of J_{pl} is not essential, as long as consistency in modelling details and result extraction is maintained. All FEA cases were run under a small-strain formulation using C3D20 elements.

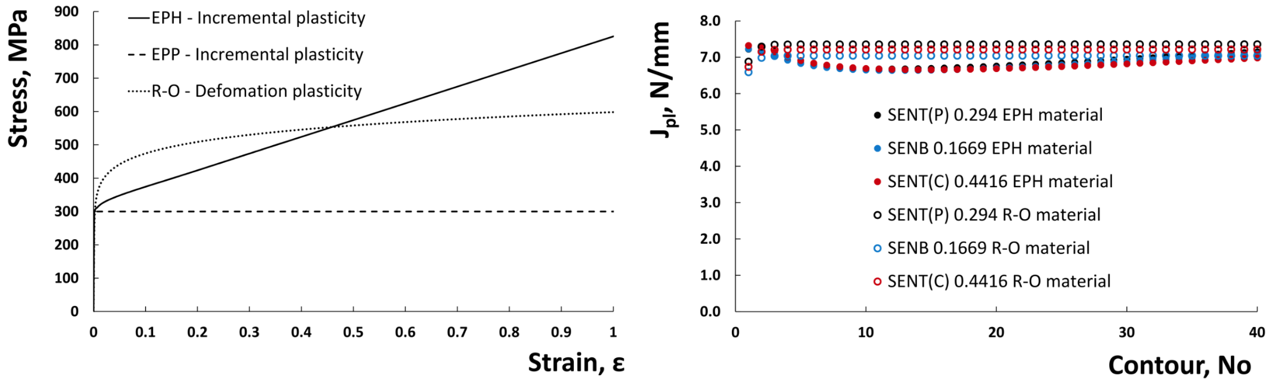

(a) (b)

Figure 6: J_{pl} values from incremental and deformation plasticity models: (a) stress-strain curves, (b) J_{pl} contour dependence curves of SENB and SENT specimens from Section 6.3 and 6.4 at $L_r = 1.0$ for R-O and EPH materials

4.2.1. Validation against GE-EPRI solutions

Finite element elastic-plastic models under plane strain conditions were validated against the GE-EPRI handbook [39] for SENB and SENT(P) geometries with α=a/W=0.25. GE-EPRI handbook solutions were derived for a R-O material as can be seen from Eq. (2). Therefore, for validation against GE-EPRI solutions only, a R-O material model, which is implemented in Abaqus within the deformation plasticity option, was used. Results are presented in Fig. 7. The elastic-plastic integral $\mathrm{J_{pl}}$ for both geometries is calculated according to:

$$\mathrm{J_{pl}} = \frac{[\mathrm{K_I(a_e)}]^2}{\mathrm{E'}} + \mu\sigma_\mathrm{y}\epsilon_0(\mathrm{W}-\mathrm{a})\mathrm{h_1}\left(\mathrm{L_r}\right)^{\mathrm{n}+1} \tag{2}$$

where $\mathrm{E'} = \mathrm{E}/(1-\nu^2)$ for plane strain, E is Young's modulus and ν is Poisson's ratio, and $\epsilon_0 = \sigma_\mathrm{y}/\mathrm{E}$. The coefficients μ and n are parameters for the Ramberg-Osgood material model used:

$$\frac{\epsilon}{\epsilon_0} = \frac{\sigma}{\sigma_\mathrm{y}} + \mu\left(\frac{\sigma}{\sigma_\mathrm{y}}\right)^{\mathrm{n}} \tag{3}$$

The values of n=10, μ=2/3, E=200 GPa, ν=0.3 and σ_y=300 MPa were used in FEA. The effective crack length, $\mathrm{a_e}$, is calculated taking into account the plastic zone size:

$$\mathrm{a_e} = \mathrm{a} + \phi \mathrm{r_y} \tag{4}$$

where plastic zone size for plane strain is calculated from:

$$\mathrm{r_y} = \frac{1}{6\pi}\left[\frac{\mathrm{n}-1}{\mathrm{n}+1}\right]\left(\frac{\mathrm{K_I}}{\sigma_\mathrm{y}}\right)^2 \tag{5}$$

and the function ϕ is:

$$\phi = \frac{1}{1 + \mathrm{L}_\mathrm{r}^2} \tag{6}$$

For the SENB specimen, h_1=0.523 and for SENT(P), h_1=2.17 [39].

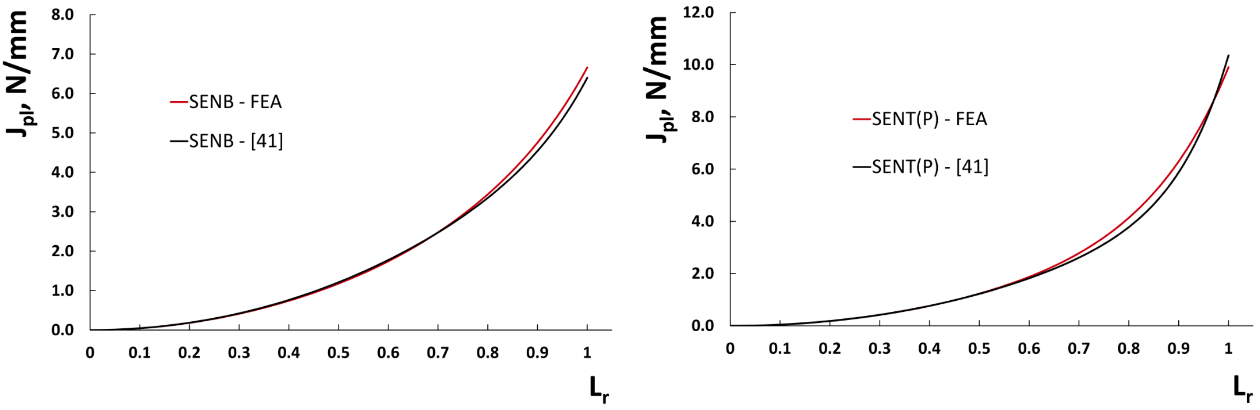

(a) (b)

Figure 7: Comparison of finite element results with EPRI procedure: (a) SENB sample with α=0.25, (b) SENT(P) sample with α=0.25

It is apparent from Fig. 7 that close agreement between the current finite element analyses and the EPRI solutions is obtained, giving confidence in the elastic-plastic analysis results.

4.2.2. Further validation using the load parameter m

For FEA reported in [40], the load parameter, m, as defined in Eq. (7) below, at which strict SSY conditions apply and there is no constraint loss, depends on hardening coefficient and varies from 175 to 340 for plane strain SENB samples with a/W = 0.5, with essentially elastic response up to the limit load based on the yield stress. The FEA in reference [40] were carried out using a power-law material model with modification of the non-linear part of the stress-strain curve starting at 0.95(σ_y/E). FEA analyses with a R-O material (n=20, α=0.1) for a plane strain SENB sample with a/W=0.5 have been performed to compare m values with those from reference [40]. With a yield strength of 300 MPa used in the current work and m=340 from reference [40], J_{pl} results in 4.41 N/mm according to the relationship

$$J_{pl} = \frac{(W - a)\sigma_y}{m} \tag{7}$$

The FEA under $L_r = 1.0$ resulted in J_{pl}=4.38 N/mm, which leads to m=342, confirming the accuracy of the current modelling in SSY conditions. Further, in the work the models were run with EPP and EPH materials to obtain larger levels of yielding.

5. The influence of T-stress on the development of plasticity and the J-integral

To assess the methodology of Section 2, a number of SENB specimens were chosen with different sizes and different crack depths such that the values of elastic J-integral, J_{el}, (obtained from the stress intensity factor solutions in the Appendix) would be the same for loads equal to the corresponding limit load (again obtained from the solutions in the Appendix) in each case. The selected geometries and loads are listed in Table 1. The table also lists values of the T-stress at the limit load ($L_r = 1.0$) and it can be seen that these are very different in different cases. In particular, SENB specimens were chosen to cover both negative and positive T-stress values, Fig. 8a.

Results from elastic-plastic analyses are shown in Fig. 8b for an EPH material model with the J_{pl} values at the limit load listed in Table 1. The results show that for positive T-stresses, the development of J with increasing load (increasing L_r) is largely independent of T-stress (constraint) when specimens are matched in the way selected. However, for negative T-stress, i.e. low constraint, there is a dependence of J development on constraint with the maximum value of J_{pl} obtained for the lowest constraint case with α=0.1. This suggests that when using a failure assessment diagram method (i.e. using a constraint-independent curve to estimate J_{pl}/J_{el}) there may be reduced conservatism in the estimate of J for low constraint cases and this is explored further in the remainder of this paper.

Table 1: Different size SENB specimens with fixed J_{el} values

Specimen	α	a, mm	W, mm	H, mm	P_L, N	J_{el}, N/mm	T, MPa	J_{pl}, N/mm
SENB 0.1	0.1	1.04	10.4	41.6	4381	3.647	-175.8	6.84
SENB 0.2	0.2	1.63	8.15	32.6	2755	3.66	-95.45	5.18
SENB 0.45	0.45	4.29	9.54	38.16	1525	3.655	14.48	4.53
SENB 0.6	0.6	7.51	12.51	50.04	1057	3.654	49.25	4.44
SENB 0.7	0.7	11.41	16.3	65.2	775	3.658	65.58	4.43

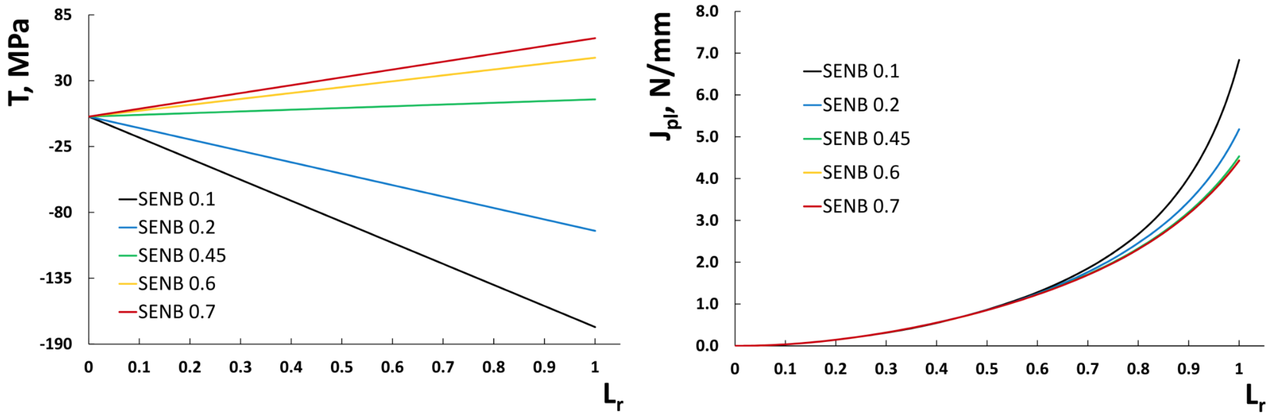

(a) (b)

Figure 8: The influence of T-stress on J_{pl} values in SENB specimens: (a) Different T-stress values for a fixed value of $J_{el} = 3.6$N/mm at $L_r = 1.0$; (b) J_{pl} curves with EPH material for different constraint levels

6. Development of plasticity in specimens in plane strain conditions

6.1. Shallow-cracked SENB-SENT(C)

It can be seen from Fig. 5b, that β_T values for SENB and SENT(C) samples are almost the same at α=0.1. Therefore, it was decided to run a matching exercise at this intersection point. A SENB sample with dimensions of 10 × 10 × 40 mm was chosen as the reference geometry and the size of the SENT(C) specimen was calculated to match the T-stress and J_{el} values of the SENB specimen according to the method of Section 2. The selected dimensions for the SENT(C) specimen are given in Table 2. That the T-stress and J_{el} values are matched is confirmed by the results in Fig. 9a and Fig. 9b.

Table 2: Summary of analysis parameters for SENB-SENT(C) shallow cracks

Parameter	**Specimen**		
	SENB	SENT(C)	SENT(C)-c
α	0.1078	0.1078	0.091
a, mm	1.078	1.9566	1.9656
W, mm	10	18.15	21.6
H, mm	40	90.75	108
B, mm	5	5	5
$\mathrm{P_L}$, N	4152	28048	33652
$\mathrm{L_r}$	1	1	0.99
$\mathrm{J_{el}}$, N/mm (FEA)	3.65	3.67	3.66
T, MPa (FEA)	-168.49	-168.03	-168.15
$\mathrm{J_{pl}}$, N/mm (FEA with EPH)	6.59	7.29	6.57
$\mathrm{J_{pl}}$, N/mm (FEA with EPP)	6.79	18.64	7.35

From an elastic-plastic analysis with an elastic-perfectly plastic (EPP) material it was found that the $\mathrm{J_{pl}}$ curve of the SENT(C) specimen with α=0.1078 increases rapidly at $\mathrm{L_r}$ approximately equal to 0.98. This indicates that the limit load of the finite element model is slightly lower than the theoretical limit load. The theoretical limit load solution was therefore reduced resulting in $\mathrm{L_r}$ value of 0.99 (Table 2) and the matching specimen size was recalculated with $\mathrm{L_r}$ fixed to 0.99 leading to a specimen, SENT(C)-c, with α=0.091, i.e. a smaller relative crack length. Because of the limit load reduction parameter α has to be reduced as well in order to maintain the same level of constraint. Accordingly, specimen width, W, then has to be adjusted to ensure the same stress intensity factor. After recalculation the limit load has changed from 28047.8 to 33652.3 N. In terms of crack tip constraint and stress intensity factor SENT(C)-c with α=0.091 is identical to SENT(C) with α=0.1078 (Fig. 9a and Fig. 9b).

The adjustment of $\mathrm{L_r}$ and specimen size recalculation for the reference SENB geometry was not performed as the SENB 0.1078 curve (Fig. 9c) did not show the rapid increase in $\mathrm{J_{pl}}$. However, in the case of the SENB sample, fully plastic conditions at the crack tip can be reached at a slightly higher load than the theoretical limit load. The following example demonstrates it. Increasing the calculated SENB 0.1078 limit load by 2% (from 4152.4 to 4235.5 N) and performing calculations up to this limit load then led to a rapid change in the $\mathrm{J_{pl}}$ curve of the SENB 0.1078 $\mathrm{L_r}$=1.02 specimen at the modified limit load as is clearly visible in Fig. 9c. In this case the sample size for both limit load cases remained the same. Further in Section 6 limit load and specimen size was only corrected for SENT specimens.

Analyses were then performed with the elastic-plastic hardening (EPH) model of Fig. 6a and results are shown in Fig. 9d. It can be seen that the development of J with normalised load for the two specimens is in very close agreement, even more so when the corrected SENT(C)-c specimen is used. Thus the method of Section 2 can be used with an identical FAD for the two geometries.

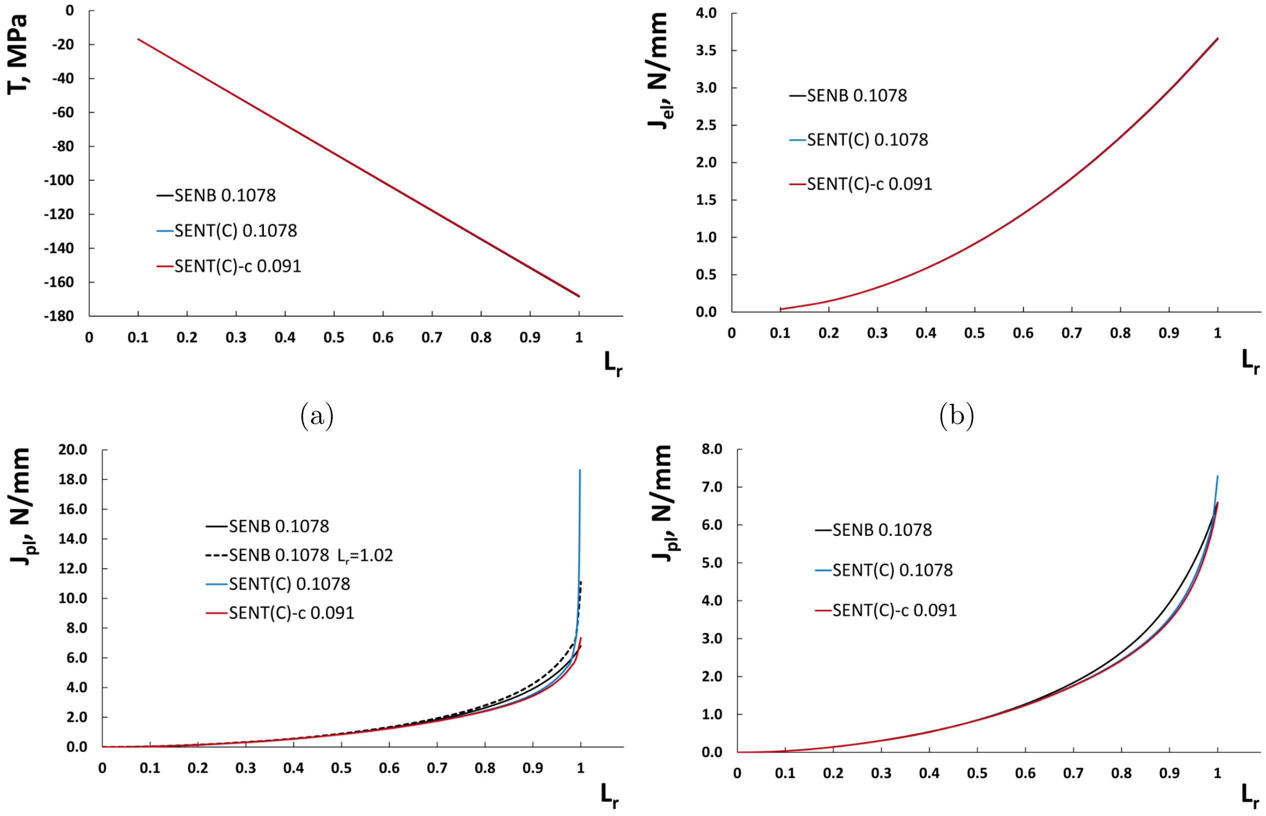

(a) (b)

(c) (d)

Figure 9: SENB-SENT(C) matching for shallow cracks. (a) T-stress values at limit load (b) J_{el} values at limit load (c) J_{pl} values at limit load using EPP material model (d) J_{pl} values at limit load using EPH material model

6.2. *Deeper-cracked SENB-SENT(C)*

Guided by Fig. 5b, matching specimens according to the method of Section 2 were chosen for SENB with α=0.1669 and SENT(C) with α=0.5 (Table 3, Fig. 10a and Fig. 10b). Finite element analysis with an EPP material indicated that fully plastic condition for the SENT specimen were reached at approximately 0.95L_r (Fig. 10c) and therefore the theoretical limit load solution was reduced leading to L_r of 0.95 (Table 3) and a corrected SENT(C)-c size with α=0.44 was obtained. The development of J for this specimen is in almost perfect agreement with that for the SENB specimen (Fig. 10b), confirming as in Section 6.1 that the method of

Section 2 is valid without any modification to the FAD.

Table 3: Summary of analysis parameters for SENB-SENT(C) deeper crack

Parameter	**Specimen**		
	SENB	SENT(C)	SENT(C)-c
α	0.1669	0.5	0.4416
a, mm	1.669	3	3.11328
W, mm	10	6	7.05
H, mm	40	30	35.25
B, mm	5	5	5
P_L, N	3665	5196	6478
L_r	1	1	0.95
J_{el}, N/mm (FEA)	4.35	4.33	4.33
T, MPa (FEA)	-118.97	-118.64	-118.77
J_{pl}, N/mm (FEA with EPH)	6.64	8.41	6.66
J_{pl}, N/mm (FEA with EPP)	6.72	16.58	7.47

The SENB limit load solution was also checked by increasing the load by 3% to check whether fully plastic conditions occurred. As in Section 6.1 for the SENB 0.1078 specimen the size of the SENB 0.1669 specimen was not modified. As can be seen from Fig. 10c, the J_{pl} curve of SENB 0.1669 L_r=1.03 changes the slope severely. For the two SENB specimens, of Section 6.1 and this section, the theoretical limit load of Appendix A is slightly lower than that required to reach fully plastic conditions in the finite element models.

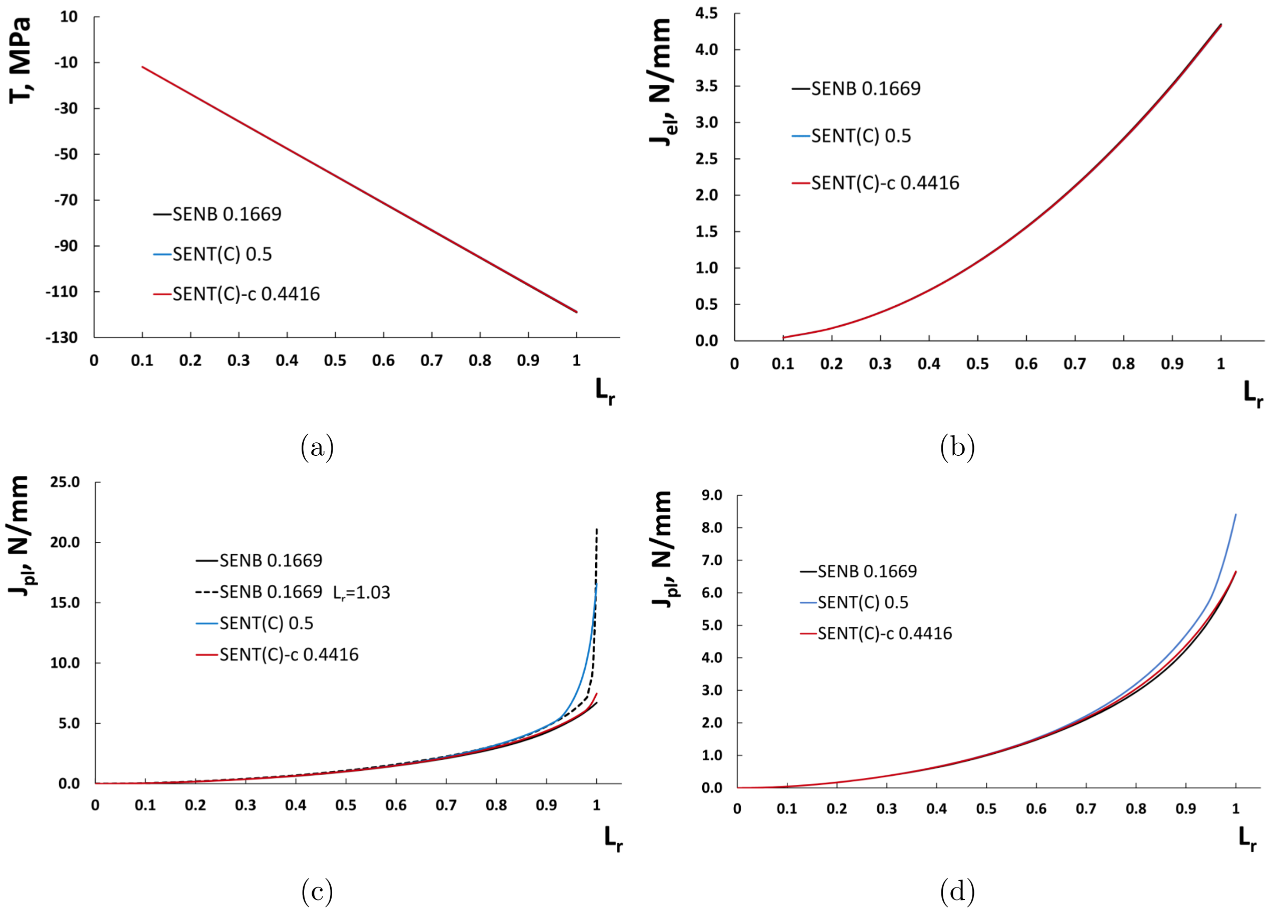

(a) (b)

(c) (d)

Figure 10: SENB-SENT(C) deeper cracks. (a) T-stress values at limit load (b) J_{el} values at limit load (c) J_{pl} values at limit load using EPP material model (d) J_{pl} values at limit load using EPH material model

6.3. Shallow cracked SENB-SENT(P)

The influence of pin-type loading has also been analysed for the SENT sample, by using the same reference SENB geometry as in Section 6.1. The elastic matching exercise of Section 2 resulted in a sample width, W=17.8 mm (Table 4), for the SENT(P) geometry, slightly smaller than W=18.15 mm for SENT(C) (Table 2).

Finite element analysis with an EPP material again indicated that fully plastic conditions for the SENT specimen were reached at a load different from the theoretical limit load and a corrected SENT(P)-c size with W=28.84 mm, larger than the width of the corrected SENT(C)-c sample, was obtained. In this case the shape of the J_{pl} curve for analyses with both EPP and EPH materials does not perfectly match the J_{pl} curve of the SENB 0.1078 sample (Figs 11c, 11d), but at L_r=1.0 almost identical values of J_{pl} are obtained.

Table 4: Summary of analysis parameters for SENB-SENT(P) shallow cracks

Parameter	**Specimen**		
	SENB	SENT(P)	SENT(P)-c
α	0.1078	0.1078	0.069
a, mm	1.078	1.9188	1.99
W, mm	10	17.8	28.84
H, mm	40	213.6	346.08
B, mm	5	5	5
P_L, N	4152	27104	44750
L_r	1	1	0.968
J_{el}, N/mm (FEA)	3.65	3.66	3.66
T, MPa (FEA)	-168.49	-168.532	-167.38
J_{pl}, N/mm (FEA with EPH)	6.59	8.78	6.53
J_{pl}, N/mm (FEA with EPP)	6.79	9.87	6.72

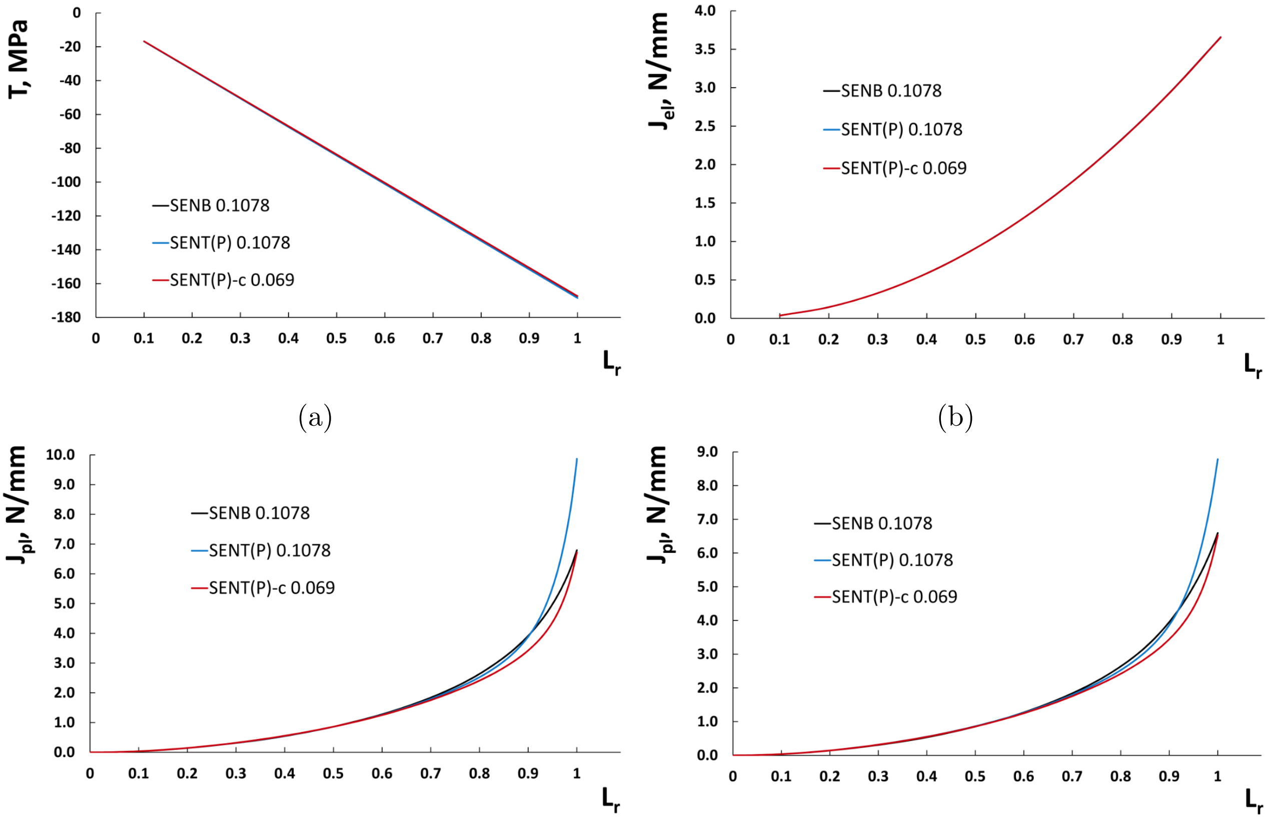

(a) (b)

(c) (d)

Figure 11: SENB-SENT(P) shallow cracks. (a) T-stress values at limit load (b) J_{el} values at limit load (c) J_{pl} values at limit load using EPP material model (d) J_{pl} values at limit load using EPH material model

6.4. Deeper cracked SENB-SENT(P)

Another matching exercise using the SENT(P) sample was performed for the reference SENB 0.1669 geometry used in Section 6.2. This resulted in an SENT(P) geometry with α=0.336 and width, W=7.35 mm (Table 5, Figs. 12a, 12b). Again a limit load correction was required leading to an increase in width to W=10.2 mm and a relative crack length change from 0.336 to 0.294, Table 5. This led to a perfect match of J_{pl} curves for both EPP and EPH materials, Figs 12c, 12d.

For the SENT(P) comparisons with the SENB specimens, it was decided to compare strains at the crack tip as well as J values. Fig. 13 shows elastic-plastic strain values in the parallel and transverse directions with respect to the crack faces. Total strain values, which are the sum of elastic and plastic strains, were taken at the nodes at the radius of 0.5 mm around the crack tip. In Fig. 13 the point with coordinate $\varphi = 0°$ lays on the crack face line at 0.5 mm away from the crack tip (position "Start" in Fig. 1c). The point with coordinate $\varphi = 180°$ is located at 0.5 mm ahead from the crack tip (position "End" in Fig. 1c). It can be see that for the corrected SENT(P) geometry of Section 6.3, strain values are much closer to those of the SENB sample than those for the uncorrected SENT geometry, Fig.13a. Similar analyses for SENB 0.1669 and SENT(P)-c 0.294 specimens (Fig. 13b) showed almost identical agreement. It is possible that the small differences in Fig. 13a are a result of the small differences in the J versus load curves of Fig. 11d.

Table 5: Summary of analysis parameters for SENB-SENT(P) deeper cracks

Parameter	**Specimen**		
	SENB	SENT(P)	SENT(P)-c
α	0.1669	0.336	0.294
a, mm	1.669	2.4696	2.9988
W, mm	10	7.35	10.2
H, mm	40	88.2	122.4
B, mm	5	5	5
P_L, N	3665	7165	9914
L_r	1	1	0.898
J_{el}, N/mm (FEA)	4.35	4.35	4.35
T, MPa (FEA)	-119	-118.5	-118.7
J_{pl}, N/mm (FEA with EPH)	6.64	9.91	6.66
J_{pl}, N/mm (FEA with EPP)	6.72	11.44	6.88

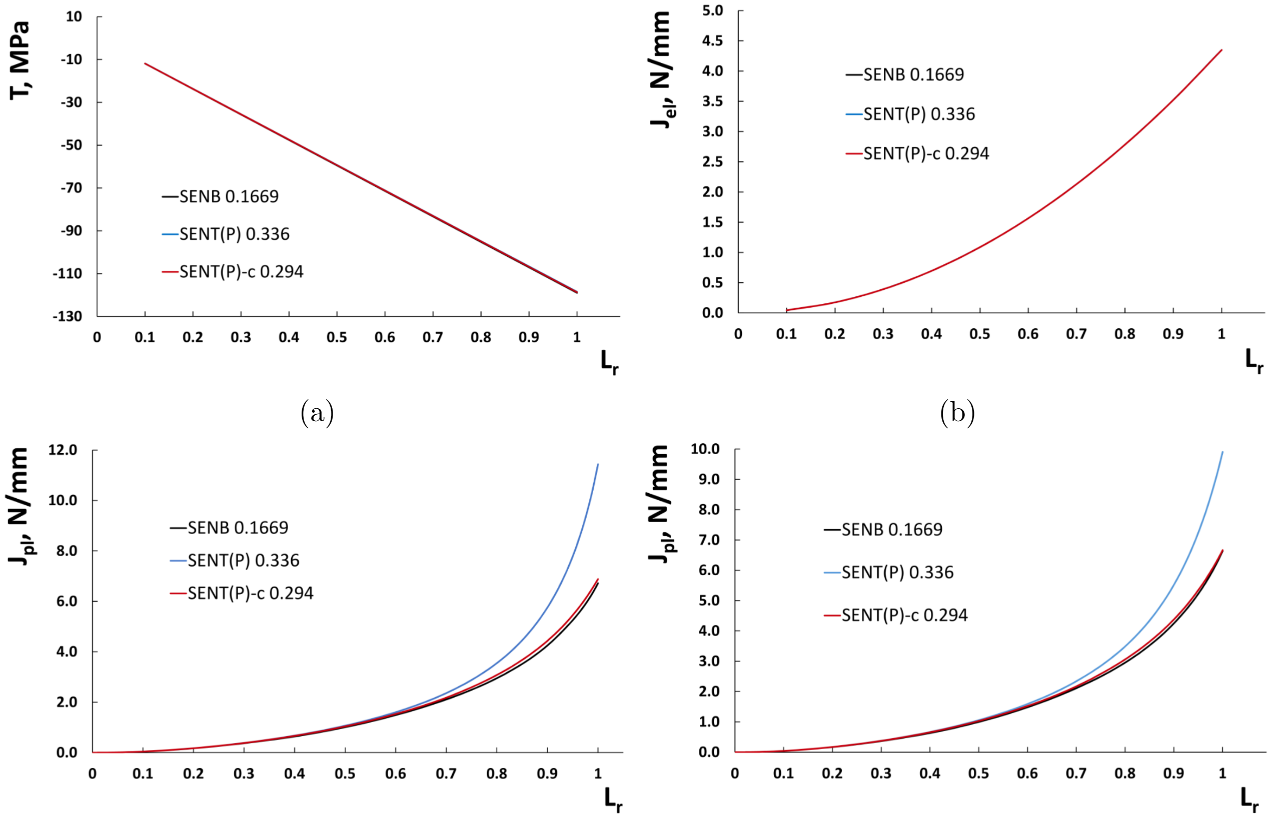

(a) (b)

(c) (d)

Figure 12: SENB-SENT(P) deeper cracks. (a) T-stress values at limit load (b) J_{el} values at limit load (c) J_{pl} values at limit load using EPP material model (d) J_{pl} values at limit load using EPH material model

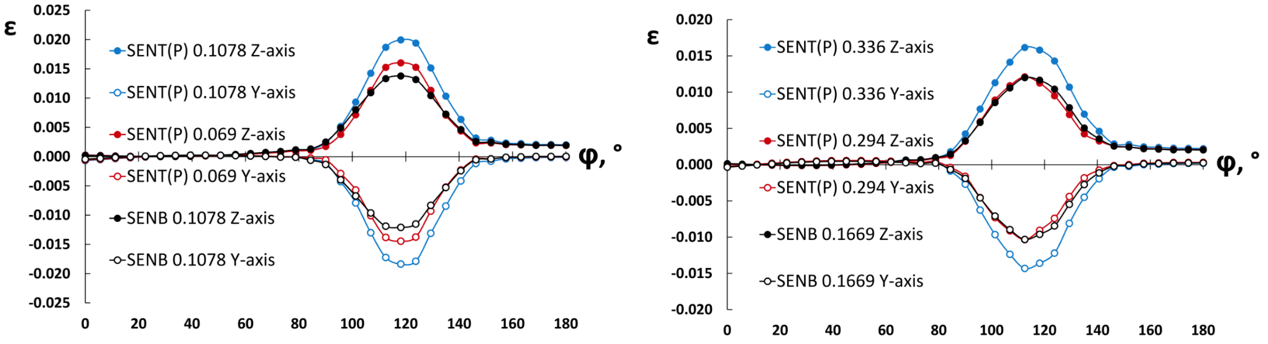

(a) (b)

Figure 13: Elastic-plastic strain distribution around the crack tip at the distance of 0.5mm for SENB and SENT(P) samples: (a) SENB 0.1078, SENT(P) 0.1078 and SENT(P)-c 0.069, (b) SENB 0.1669, SENT(P) 0.336 and SENT(P)-c 0.294

7. Cracked pipes and matching specimens

7.1. Circumferentially through-wall thickness cracked pipe and plane strain specimens

A more general matching exercise was performed using a reference SENB specimen with α=0.156, both SENT(C) and SENT(P) specimens and a through-wall cracked pipe. Circumferential cracks in pipes might appear due to high bending moment and develop from surface to through-wall cracks. The TWC pipe geometry is a low-constraint geometry as was found earlier from finite element analysis [34]. Fracture toughness obtained from TWC pipe would be different from that obtained from a standard specimen. Therefore, the TWC pipe is a suitable geometry for which the approach can be demonstrated. The specimens were analysed in plane strain and the dimensions of the matching specimens and pipe are given in Table 6. As in Section 6, corrections were made for the SENT specimen limit loads. TWC pipes were also simulated under limit load which according to the experimental data from [41] was load at fracture for 8-inch TWC pipes subjected to bending moment, while 16-inch pipes failed at $\mathrm{L_r} < 1.0$. The comparisons in Fig. 14a show similar agreement between the SENT and SENB specimens as obtained in the analyses in Section 6, but the $\mathrm{J_{pl}}$ values of all plane strain specimens are lower than that of TWC pipe. The values of $\mathrm{J_{pl}}$ for the TWC pipe were taken on the mid-plane of the wall. Fig. 14b shows very excellent matching of the $\mathrm{J_{pl}}$ curves for the three plane strain specimens, when limit load corrections have been made, but still show an increased $\mathrm{J_{pl}}$ for the TWC pipe. As with the results in Section 5, this suggests that when using a failure assessment diagram method there may be reduced conservatism in the estimate of $\mathrm{J_{pl}}$ for pipe geometries than test specimens even when all are low constraint cases.

Table 6: Summary of analysis parameters for TWC pipe and plane strain samples

Parameter	**Specimen**					**TWC Pipe**
	SENB	SENT(C)	SENT(C)-c	SENT(P)	SENT(P)-c	
$\alpha = \theta/\pi$	0.156	0.426	0.37	0.312	0.269	0.22
a, mm or θ,°	4.134	7.23345	7.6775	6.3336	7.5724	39.6
$W(R_m)$, mm	26.5	16.98	20.75	20.3	28.15	10
H, mm	106	84.9	103.75	243.6	337.8	200
B(t), mm	5	5	5	5	5	2
P_L, N or M_L, Nmm	9960	1688	21510	21042	29245	149818
L_r	1	1	0.95	1	0.907	1
J_{el}, N/mm (FEA)	11.3	11.31	11.28	11.3	11.3	11.29
T, MPa (FEA)	-127.3	-127	-127.6	-126.6	-126.3	-127.4
J_{pl}, N/mm (FEA with EPH)	17.11	23.58	16.93	25.32	17.38	27.74

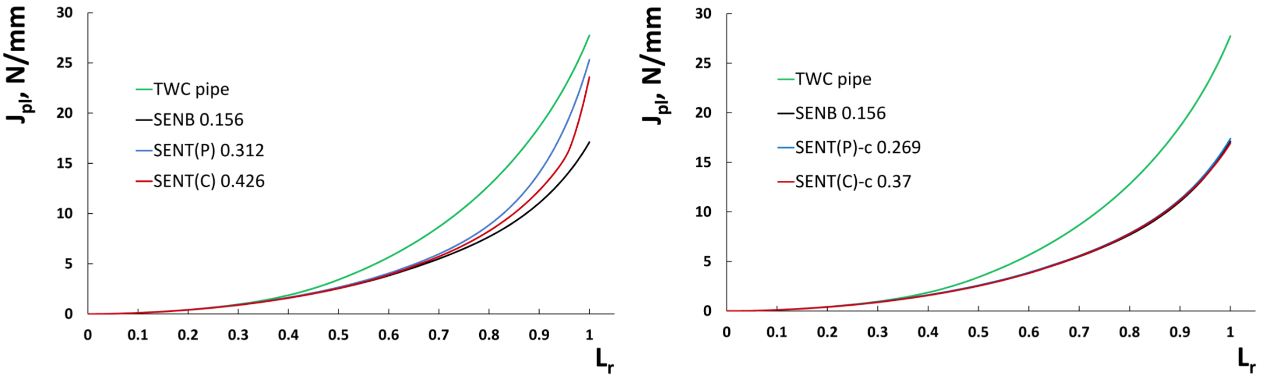

(a) (b)

Figure 14: TWC pipes and plane strain specimens using EPH material option: (a) J_{pl} values at limit load for plane strain specimens and TWC pipe, (b) J_{pl} values for TWC pipe, SENB and corrected SENT(P)-c, SENT(C)-c

7.2. Circumferentially through-wall thickness cracked pipe and three-dimensional test specimen specimens

In practice, laboratory specimens are three-dimensional (3D) with a stress state between plane strain and plane stress conditions. Therefore, the limit load is lower than the plane strain limit load but higher than that in plane stress. For example, the plane stress limit load for the SENT(C) specimen is 1.154 times lower than the plane strain limit load [27]. In 3D specimens the stress intensity factor and T-stress also vary along the thickness as demonstrated in [42, 43, 44], where solutions for stress intensity factor and T-stress at the thickness mid-plane are provided.

To assess the effect of out-of plane conditions, three-dimensional analyses were performed with the boundary conditions previously applied to create plane strain conditions removed. The applied loads remained the same as for the plane strain specimens (Table 6). It was found that J_{pl} values increased drastically when 3D specimens were subjected to the limit load calculated for plane strain conditions, as can be seen from Fig. 16a, where the scale on the ordinate is an order of magnitude greater than that in Fig. 14a. The reason for high J_{pl} values for specimens in Fig. 16a is the small B/W ratio. For instance, in the case of the 3D SENB 0.156 sample, B/W = 0.19 (Table 7), the stress state is more similar to that in plane stress conditions. Larger B/W ratio reduces the plane stress effect. Specimens with B/W=1.0 or B/W=0.5 are usually used in fracture toughness testing [45, 46]. Two cases from the literature are described next.

Pre-cracked Charpy V-notch specimens (B=10 mm, W= 10 mm, S/W=4) cut from A572 Gr 50 steel were tested for fracture toughness at -20 °C temperature in the work [45]. For A572 Gr 50 steel, σ_y at -20 ° C is 407 MPa and Young's modulus E=201 GPa. Fourteen specimens were tested in total (Table 4 in [45]) with initial crack length from 4.9 to 5.5 mm (average 5.12 mm). The average fracture toughness obtained was 71.64 N/mm (from 40 to 107 N/mm). Measured load at fracture was approximately 4.12 kN at -20 °C for the specimens with a/W=0.5 (see Fig. 4b in [45]). The calculated plane strain limit load using Eq. (A.2) and $\sigma_y = 407$ MPa is 3.58 kN, which is significantly lower than the experimental load of 4.12 kN at fracture. Finite element analysis shows that in plane strain conditions with and elastic-perfectly plastic material and an elastic limit of $\sigma_y = 407$ MPa, the limit load is reached at load 4% higher than 3.58 kN, which is in good agreement with Eq. (A.2). At this point the trajectory of J_{pl} curve changes severely (Fig. 15a) and the ligament becomes fully plastically deformed (Fig. 15b) indicating that the limit load has been reached [47]. The engineering stress-strain curve of A572 Gr 50 steel presented in in Fig. 2a of [45] exhibits a yield plateau and enters the hardening stage with hardening exponent n=8.0 at a strain value of about 0.01. Plane strain FEA analysis with an EPH material with a yield point offset, where σ_y=407 MPa at 0.01 strain, resulted in J_{pl}=48.31 N/mm at a load 20% higher than the nominal limit load, 1.2 × 3.58 kN=4.3 kN (Fig. 15a). For a 3D specimen, a lower load of 4.12 kN, equal to the experimental load at fracture, resulted in a similar averaged across thickness J_{pl} value of 50.1 N/mm. This is higher than the minimum experimental value of 40 N/mm, but lower than the average value of 71.64 N/mm. However, the maximum J_{pl} value of 59.13 N/mm at the specimen's mid-plane (Fig. 15a) is higher than the averaged across thickness value.

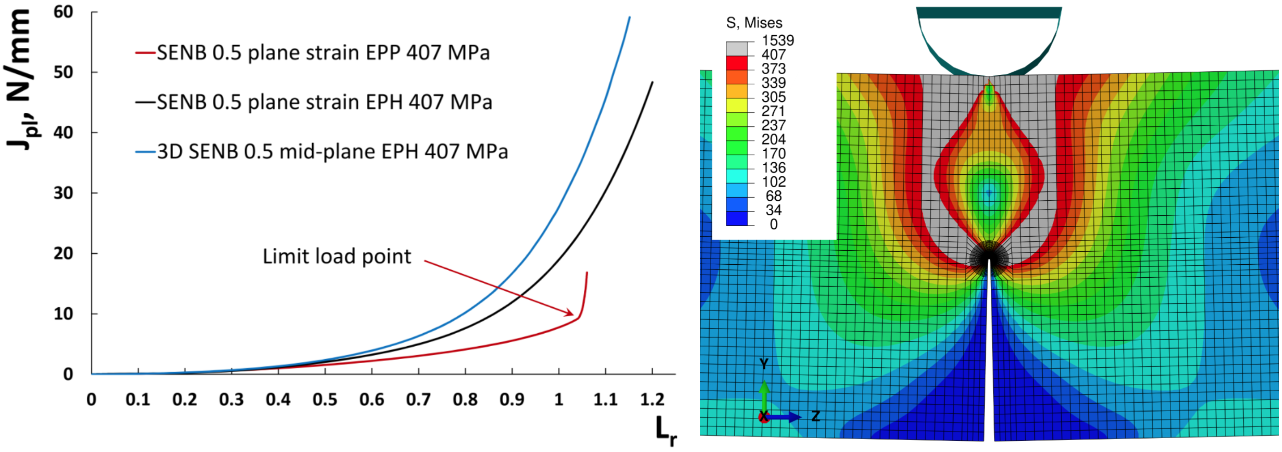

(a) (b)

Figure 15: Limit load analysis of SENB 0.5 10 × 10 × 40 mm specimen when σ_y = 407 MPa: (a) J_{pl} curves under full plastic zone penetration into the ligament for an EPP and EPH materials with yield point offset , (b) full plastic zone (grey contour with values > 407 MPa) penetration into the ligament

Fracture toughness data of SENB specimens with B/W=0.5 at 20° C temperature are given in [46]. Six specimens (B=12.5 mm, W=25 mm, S/W=4) with a/W = 0.5 of CrMo steel JIS SCM440 were tested. The experimental load at fracture varied from 12.2 to 15.7 kN (average 14.3 kN) and fracture toughness varied from 27.0 to 69.1 N/mm (average 53.48 N/mm). Reported material properties at 20° C temperature are: σ_y = 458.5 MPa at 0.2% offset, hardening exponent n = 4.77 and E=216 GPa. The offset of 0.2% results in strain value of 0.0041 at σ_y = 458.5 MPa. The calculated limit load according to the plane strain limit load solution (Eq. (A.2)) with σ_y = 458.5 MPa is 12.62 kN. The FEA with an EPH material showed that the ligament is fully plastically deformed at a load 14% higher than the nominal limit load, 1.14 × 12.62 kN=14.39 kN and the averaged across thickness J_{pl} = 62.42 N/mm at this load. This value is higher than the average fracture toughness of 53.48 N/mm, but lower than the maximum experimental fracture toughness of 69.1 N/mm. The numerical load applied of 14.39 kN is close to the experimental average load at fracture of 14.3 kN.

These two literature cases described above and the associated finite element analysis which have been performed show that the experimental load at fracture is often close to but in excess of the limit load from a plane strain. The numerical J-integral values at the fracture load depend on the yield point offset. For an elastic-perfectly plastic material, the yield point offset is equal to zero and the J-integral value at the limit load is close to that obtained from an elastic material. A material with significant yield point offset accumulates more plastic work at the limit load and the J-integral value is greater than that calculated elastically. This is particular visible from Fig. 15a, where the plane strain curve with an EPP material (σ_y=407 MPa at $\sigma_\mathrm{y}/\mathrm{E} = 0.002$ strain) at $\mathrm{L_r} = 1.04$ reaches $\mathrm{J_{pl}} = 9.72$ N/mm and the plane strain curve with an EPH material (σ_y=407 MPa at 0.01 strain) at $\mathrm{L_r} = 1.2$ reaches $\mathrm{J_{pl}} = 48.31$ N/mm. In the case of the EPH material, the remaining ligament becomes fully plastically deformed at the higher load, $\mathrm{L_r} = 1.2$.

Now the mid-plane $\mathrm{J_{pl}}$ curves for all 5 mm thickness ($\mathrm{B/W} < 0.3$) specimens greatly exceed the TWC pipe curve when using the plane strain limit loads to normalise the test specimen results. The limit load of a thin specimen is lower than the plane strain limit load. Therefore, the B/W ratio for 3D specimens was increased to a standard 1.0 value in order to reduce plane stress effects, which are quite complex to take into account as limit load solutions for variable specimen thickness are not readily available. The increased thickness reduces J-integral value. For the 3D samples with B/W=1.0, the limit load used to normalise the results was then reduced until the mid-plane $\mathrm{J_{pl}}$ value was matched (Fig. 16b). Although the $\mathrm{J_{pl}}$ values at $\mathrm{L_r}$=1.0 must now match for the TWC pipe and all 3D specimens, it is found that the $\mathrm{J_{pl}}$ curves for SENB, SENT(C)-c and SENT(P)-c specimens exhibit very similar shapes, the TWC is rather different.

Table 7: Summary of analysis parameters for TWC pipe and 3D specimens

Parameter	**Specimen**						**TWC Pipe**
	SENB	SENB-c	SENT(C)	SENT(C)-c	SENT(P)	SENT(P)-c	
$\alpha = \theta/\pi$	0.156	0.147	0.426	0.28	0.312	0.23	0.22
a, mm or θ,°	4.134	4.1748	7.2335	6.9776	6.3336	7.13	39.6
$W(R_m)$, mm	26.5	28.4	16.98	24.92	20.3	31	10
H, mm	106	113.6	84.9	124.6	243.6	279	200
B(t), mm	5	28.4	5	24.92	5	31	2
P_L, N or M_L, Nmm	9960	58764	16881	144201	21042	214819	149818
L_r	1	0.95	1	0.931	1	0.9	1
J_{el}, N/mm (FEA)	12.76	11.27	12.77	11.24	12.72	11.31	11.29
T, MPa (FEA)	-103.4	-126.9	-104.3	-126.4	-104.6	-126.7	-127.4
J_{pl}, N/mm (FEA with EPH)	299.9	27.96	122.6	27.38	458.6	27.38	27.74

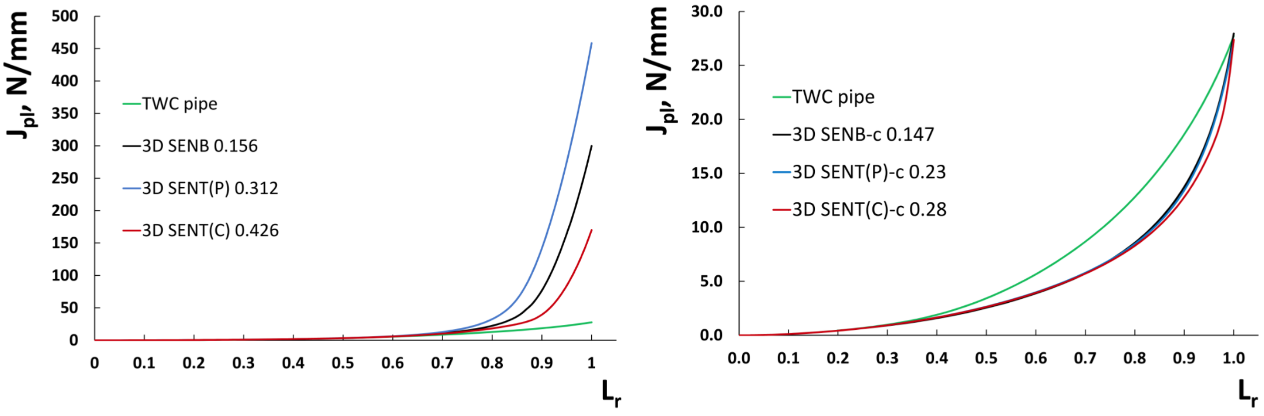

(a) (b)

Figure 16: TWC pipe and 3D specimens using EPH material option: (a) 3D specimens subjected to plane strain limit loads (b) 3D samples subjected to corrected plane strain limit loads

7.3. Fully-circumferential internally cracked pipe and matching specimens

Similar exercises to those of Sections 7.1 and 7.2 have been performed for a fully-circumferentially cracked pipe. The FCC pipe is a convenient pipe geometry to demonstrate the approach, because K_I or T-stress is a single value at any point of circumferential crack front. Conversely, in a TWC pipe T-stress and SIF vary across the wall thickness. Table 8 summarises the analysis parameters for the FCC pipe and matching plane strain and 3D specimens. In this case, the SENB plane strain J_{pl} curve almost matches the FCC curve while the SENT(C) and SENT(P) J_{pl} curves are a little higher (Fig. 17a). After limit load correction, the J_{pl} curves of all matching specimens are in agreement with the FCC pipe curve (Fig. 17b).

Table 8: Summary of analysis parameters for FCC pipe and specimens

Parameter	**Specimen**						**FCC Pipe**
	2D			3D			
	SENB	SENT(C)	SENT(P)	SENB-c	SENT(C)-c	SENT(P)-c	
α	0.16	0.44	0.32	0.135	0.248	0.2	0.6
a, mm	1.2288	2.1296	1.8496	1.3635	2.2221	2.368	3.6
W, mm	7.68	4.84	5.78	10.1	8.96	11.84	6
H, mm	30.72	24.2	69.36	40.4	44.8	106.56	140
B (R_e), mm	5	5	5	5.05	8.96	11.84	36
P_L, N	2860	4695	5873	6983	18508	31023	178802
L_r	1	1	1	0.87	0.885	0.842	1
J_{el}, N/mm (FEA)	3.3	3.29	3.29	3.24	3.26	3.29	3.28
T, MPa (FEA)	-124.2	-125.2	-124	-124.7	-125.8	-125.5	-125.6
J_{pl}, N/mm (FEA with EPH)	4.31	6.7	7.31	5.45	5.3	5.23	5.43

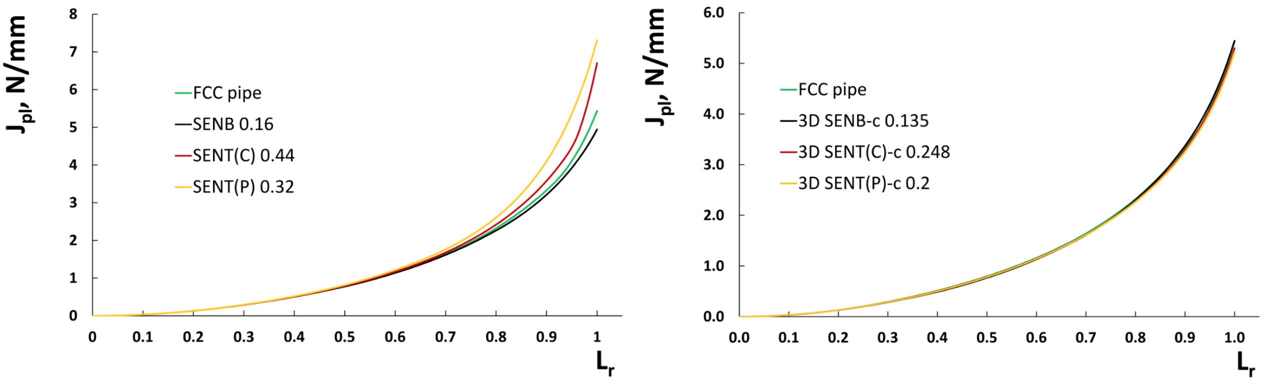

(a) (b)

Figure 17: FCC pipe and samples simulated using EPH material: (a) FCC pipe and plane strain samples, (b) FCC pipe and three-dimensional samples

8. Discussion

The current constraint correction procedure in the FAD method is based on testing of samples with different constraint levels to obtain the fracture toughness dependence on constraint. Then, according to the results obtained, the failure assessment line is adjusted. The proposed approach does not require failure assessment line adjustment, as fracture toughness is measured at the same or similar stress state as that which is present in the component of interest. The proposed approach, as has been demonstrated in the manuscript, allows selection of such a stress state by choosing appropriate non-standard specimen size and crack length.

The idea of the proposed approach is to have an analytical method allowing for similarity of stress fields in two cracked geometries. Such a method is described in this work and is based on elastic fracture mechanics parameters, stress intensity factor and T-stress. As the results of elastic finite element analysis show, the method works well for an elastic material. T-stress and stress intensity parameter match in two different geometries. When a material deforms plastically, the stress fields at the crack tip of two geometries might deviate from each other. Elastic-plastic finite element analysis helps to investigate whether the deviation, monitored by the change in $\mathrm{J_{pl}}$ integral, occurs or not. In some cases, $\mathrm{J_{pl}}$ curves from different geometries followed the same path up to limit load.

The output of elastic-plastic FE analysis depends on the analysis parameters. In the failure assessment diagram approach, a limit to the structure containing a defect being considered safe is if the service load does not exceed the collapse load. Widespread plasticity corresponds to the limit load parameter $\mathrm{L_r}$ greater than 1.0. However, here a small-strain formulation was used in elastic-plastic analysis as the applied load was always equal to the limit load. A non-linear geometrical effect option could be considered for higher $\mathrm{L_r}$ values, where stress is greater than yield strength. The influence of constraint on fracture load is however greatest when the load is less than that to cause widespread yielding and so analyses to higher loads are of less importance [48]. Material hardening parameters affect $\mathrm{J_{pl}}$ values, but with EPP material it is clearer to observe when the crack tip zone is fully plastically deformed. It illustrates SENB-SENT(C) example in Fig. 9. In general, under the same limit load EPP material results in higher $\mathrm{J_{pl}}$ values, than EPH.

Elastic-plastic analysis results have shown that the approach has potential for further development and validation. It should be checked experimentally how the initiation fracture toughness obtained from a modified geometry matches that obtained from a low-constraint reference geometry and whether it is less conservative compared to that measured from a high-constraint standard specimen.

9. Concluding Remarks

A method to treat constraint effects by matching the elastic T-stress and stress intensity factor in different geometries has been proposed previously. Elastic-plastic finite element analysis have been performed to examine how the approach works for elastic-plastic materials for a number of different cases. Elastic-plastic J-integral curves with increasing load have been compared up to limit load for plane strain specimens, three dimensional specimens and pipe geometries. It has been found that accurate matching can be obtained but the limit loads for SENT(C) and SENT(P) should be based on the finite element models as these lead to lower limit load values than those from theoretical solutions. For pipes, some differences from plane strain test specimens in the shapes of the J_{pl} curves as a function of increasing load were obtained for a TWC pipe but good agreement was obtained for FCC pipes. Closer agreement between specimens and TWC pipes was obtained when three dimensional specimens were used to match the pipe geometries.

References

[1] BSI, BS 7448-1: 1991-Fracture mechanics toughness tests-part 1: method for determination of K_{Ic}, critical CTOD and critical J values of metallic materials.

[2] J. Tan, G. Wang, F. Xuan, S. Tu, Correlation of creep crack-tip constraint between axially cracked pipelines and test specimens, International Journal of Pressure Vessels and Piping 98 (2012) 16 – 25. `doi:https://doi.org/10.1016/j.ijpvp.2012.06.004`.
URL `http://www.sciencedirect.com/science/article/pii/S0308016112000828`

[3] M. Panico, H. Tang, D. Fairchild, W. Cheng, ExxonMobil SENT test method and application to strain-based design, International Journal of Pressure Vessels and Piping 156 (2017) 17 – 22, sENT Fracture Toughness Testing and Its Applications to High-Strength Pipelines. `doi:https://doi.org/10.1016/j.ijpvp.2017.06.010`.
URL `http://www.sciencedirect.com/science/article/pii/S0308016117300704`

[4] Y. Chen, G. Wang, F. Xuan, S. Tu, Crack-tip constraint analyses and constraint-dependent LBB curves for circumferential through-wall cracked pipes, Nuclear Engineering and Design

285 (2015) 75 – 83. `doi:https://doi.org/10.1016/j.nucengdes.2015.01.012`.
URL `http://www.sciencedirect.com/science/article/pii/S0029549315000497`

[5] D. F. Sarzosa, C. Ruggieri, A numerical investigation of constraint effects in circumferentially cracked pipes and fracture specimens including ductile tearing, International Journal of Pressure Vessels and Piping 120-121 (2014) 1 – 18. `doi:https://doi.org/10.1016/j.ijpvp.2014.03.005`.
URL `http://www.sciencedirect.com/science/article/pii/S0308016114000350`

[6] J. Xu, Z. Zhang, E. stby, B. Nyhus, D. Sun, Effects of crack depth and specimen size on ductile crack growth of SENT and SENB specimens for fracture mechanics evaluation of pipeline steels, International Journal of Pressure Vessels and Piping 86 (12) (2009) 787 – 797. `doi:https://doi.org/10.1016/j.ijpvp.2009.12.004`.
URL `http://www.sciencedirect.com/science/article/pii/S0308016109001835`

[7] E. Berg, E. stby, C. Thaulow, B. Skallerud, Ultimate fracture capacity of pressurised pipes with defects - Comparisons of large scale testing and numerical simulations, Engineering Fracture Mechanics 75 (8) (2008) 2352 – 2366. `doi:https://doi.org/10.1016/j.engfracmech.2007.09.004`.
URL `http://www.sciencedirect.com/science/article/pii/S0013794407003529`

[8] B. r. Nyhus, M. L. Polanco, O. Orjasæther, SENT specimens an alternative to SENB specimens for fracture mechanics testing of pipelines, in: International Conference on Offshore Mechanics and Arctic Engineering, Vol. 36835, 2003, pp. 259–266.

[9] Y. Huang, W. Zhou, Effects of crack front curvature on J-R curve testing using clamped SE(T) specimens of homogeneous materials, International Journal of Pressure Vessels and Piping 134 (2015) 112 – 127. `doi:https://doi.org/10.1016/j.ijpvp.2015.05.001`.
URL `http://www.sciencedirect.com/science/article/pii/S0308016115000538`

[10] M. Chiesa, B. Nyhus, B. Skallerud, C. Thaulow, Efficient fracture assessment of pipelines. A constraint-corrected SENT specimen approach, Engineering Fracture Mechanics 68 (5) (2001) 527 – 547. `doi:https://doi.org/10.1016/S0013-7944(00)00129-6`.
URL `http://www.sciencedirect.com/science/article/pii/S0013794400001296`

[11] Y. Huang, W. Zhou, J-CTOD relationship for clamped SE(T) specimens based on three-dimensional finite element analyses, Engineering Fracture Mechanics 131 (2014) 643 – 655. doi:https://doi.org/10.1016/j.engfracmech.2014.10.007.
URL http://www.sciencedirect.com/science/article/pii/S0013794414003294

[12] L. A. Silva, S. Cravero, C. Ruggieri, Correlation of fracture behavior in high pressure pipelines with axial flaws using constraint designed test specimens. Part II: 3-D effects on constraint, Engineering Fracture Mechanics 73 (15) (2006) 2123 – 2138. doi:https://doi.org/10.1016/j.engfracmech.2006.04.004.
URL http://www.sciencedirect.com/science/article/pii/S0013794406001536

[13] A. H. Sherry, C. C. France, M. R. Goldthorpe, Compendium of T-stress solutions for two and three dimensional cracked geometries, Fatigue & Fracture of Engineering Materials & Structures 18 (1) (1995) 141–155. arXiv:https://onlinelibrary.wiley.com/doi/pdf/10.1111/j.1460-2695.1995.tb00148.x, doi:10.1111/j.1460-2695.1995.tb00148.x.
URL https://onlinelibrary.wiley.com/doi/abs/10.1111/j.1460-2695.1995.tb00148.x

[14] C. Thaulow, E. stby, B. Nyhus, Z. L. Zhang, B. Skallerud, Constraint correction of high strength steel: Selection of test specimens and application of direct calculations, Engineering Fracture Mechanics 71 (16) (2004) 2417 – 2433. doi:https://doi.org/10.1016/j.engfracmech.2004.01.003.
URL http://www.sciencedirect.com/science/article/pii/S0013794404000232

[15] P. Ding, X. Wang, An estimation method for the determination of the second elasticplastic fracture mechanics parameters, Engineering Fracture Mechanics 79 (2012) 295 – 311. doi:https://doi.org/10.1016/j.engfracmech.2011.11.010.
URL http://www.sciencedirect.com/science/article/pii/S0013794411004188

[16] V. Shlyannikov, N. Boychenko, A. Tumanov, A. Fernndez-Canteli, The elastic and plastic constraint parameters for three-dimensional problems, Engineering Fracture Mechanics 127 (2014) 83 – 96. doi:https://doi.org/10.1016/j.engfracmech.2014.05.015.
URL http://www.sciencedirect.com/science/article/pii/S0013794414001799

[17] Y. Chao, S. Yang, M. Sutton, On the fracture of solids characterized by one or two parameters: Theory and practice, Journal of the Mechanics and Physics of Solids 42 (4) (1994) 629 – 647. `doi:https://doi.org/10.1016/0022-5096(94)90055-8`.
URL `http://www.sciencedirect.com/science/article/pii/0022509694900558`

[18] N. P. O'dowd, Applications of two parameter approaches in elastic-plastic fracture mechanics, Engineering Fracture Mechanics 52 (3) (1995) 445 – 465. `doi:https://doi.org/10.1016/0013-7944(95)00033-R`.
URL `http://www.sciencedirect.com/science/article/pii/001379449500033R`

[19] P. Cui, W. Guo, Higher order J-T_Z-A_T solution for three-dimensional crack border fields in power-law hardening solids, Engineering Fracture Mechanics 222 (2019) 106736. `doi:https://doi.org/10.1016/j.engfracmech.2019.106736`.
URL `http://www.sciencedirect.com/science/article/pii/S0013794419309695`

[20] W. Guo, Three-dimensional analyses of plastic constraint for through-thickness cracked bodies, Engineering Fracture Mechanics 62 (4) (1999) 383 – 407. `doi:https://doi.org/10.1016/S0013-7944(98)00102-7`.
URL `http://www.sciencedirect.com/science/article/pii/S0013794498001027`

[21] Y. Matvienko, G. Nikishkov, Two-parameter J-A concept in connection with crack-tip constraint, Theoretical and Applied Fracture Mechanics 92 (2017) 306 – 317. `doi:https://doi.org/10.1016/j.tafmec.2017.04.007`.
URL `http://www.sciencedirect.com/science/article/pii/S0167844217300927`

[22] G. P. Nikishkov, Y. G. Matvienko, Elasticplastic constraint parameter A for test specimens with thickness variation, Fatigue & Fracture of Engineering Materials & Structures 39 (8) (2016) 939–949. `arXiv:https://onlinelibrary.wiley.com/doi/pdf/10.1111/ffe.12390`, `doi:10.1111/ffe.12390`.
URL `https://onlinelibrary.wiley.com/doi/abs/10.1111/ffe.12390`

[23] M. Gupta, R. Alderliesten, R. Benedictus, A review of T-stress and its effects in fracture mechanics, Engineering Fracture Mechanics 134 (2015) 218 – 241. `doi:https://doi.org/10.1016/j.engfracmech.2014.10.013`.
URL `http://www.sciencedirect.com/science/article/pii/S001379441400335X`

[24] Y. Matvienko, The effect of the non-singular T-stress components on crack tip plastic zone under mode I loading, Procedia Materials Science 3 (2014) 141 – 146, 20th European Conference on Fracture. `doi:https://doi.org/10.1016/j.mspro.2014.06.026`.
URL `http://www.sciencedirect.com/science/article/pii/S2211812814000273`

[25] H. Moustabchir, Z. Azari, S. Hariri, I. Dmytrakh, Experimental and computed stress distribution ahead of a notch in a pressure vessel: Application of T-stress conception, Computational Materials Science 58 (2012) 59 – 66. `doi:https://doi.org/10.1016/j.commatsci.2012.01.029`.
URL `http://www.sciencedirect.com/science/article/pii/S0927025612000560`

[26] P. Moore, H. Pisarski, SENT testing standard BS 8571 and its ongoing development, International Journal of Pressure Vessels and Piping 156 (2017) 2 – 7, sENT Fracture Toughness Testing and Its Applications to High-Strength Pipelines. `doi:https://doi.org/10.1016/j.ijpvp.2017.05.011`.
URL `http://www.sciencedirect.com/science/article/pii/S0308016116304124`

[27] R6. Assessment of the integrity of structures containing defects Revision 4, including subsequent updates to Amendment 11. Gloucester, UK: EDF Energy Generation.

[28] I. Hadley, A. Horn, Treatment of constraint in BS 7910:2013, ISO 27306 and DNVGL-RP-F108, International Journal of Pressure Vessels and Piping 169 (2019) 77 – 93. `doi:https://doi.org/10.1016/j.ijpvp.2018.11.015`.
URL `http://www.sciencedirect.com/science/article/pii/S0308016118301789`

[29] B. Standard, BS 7910: 2013+ A1: 2015 guide to methods for assessing the acceptability of flaws in metallic structures, London, UK: BSI Stand Publ.

[30] M. Gintalas, R. Ainsworth, Constraint based assessments of large-scale cracked straight pipes and elbows, in: ASME 2015 Pressure Vessels and Piping Conference, American Society of Mechanical Engineers Digital Collection, 2015.

[31] R. Ainsworth, M. Gintalas, M. Sahu, J. Chattopadhyay, B. Dutta, Failure assessment diagram assessments of large-scale cracked straight pipes and elbows, SMiRT 23 - Manchester, UK.

[32] N. Larrosa, R. Ainsworth, R. Akid, P. Budden, C. Davies, I. Hadley, D. Tice, A. Turnbull, S. Zhou, "Mind the gap" in fitness-for-service assessment procedures-review and summary of a recent workshop, International Journal of Pressure Vessels and Piping 158 (2017) 1 – 19. `doi:https://doi.org/10.1016/j.ijpvp.2017.09.004`.
URL `http://www.sciencedirect.com/science/article/pii/S0308016117301205`

[33] R. John, B. Rigling, Effect of height to width ratio on K and CMOD solutions for a single edge cracked geometry with clamped ends, Engineering Fracture Mechanics 60 (2) (1998) 147 – 156. `doi:https://doi.org/10.1016/S0013-7944(98)00009-5`.
URL `http://www.sciencedirect.com/science/article/pii/S0013794498000095`

[34] M. Gintalas, R. Ainsworth, F. Scenini, T-stress solutions for through-wall circumferential cracks in straight pipes under bending, International Journal of Pressure Vessels and Piping 152 (2017) 27 – 37. `doi:https://doi.org/10.1016/j.ijpvp.2017.04.004`.
URL `http://www.sciencedirect.com/science/article/pii/S0308016116304173`

[35] M. Smith, ABAQUS/standard users manual, version 6.9, Dassault Systemes Simulia Corp.

[36] D. Carka, C. M. Landis, On the path-dependence of the J-integral near a stationary crack in an elastic-plastic material, Journal of Applied Mechanics 78 (1).

[37] D. Stump, E. Zywicz, J-integral computations in the incremental and deformation plasticity analysis of small-scale yielding, Engineering Fracture Mechanics 45 (1) (1993) 61 – 77. `doi:https://doi.org/10.1016/0013-7944(93)90008-G`.
URL `http://www.sciencedirect.com/science/article/pii/001379449390008G`

[38] W. Brocks, I. Scheider, et al., Numerical aspects of the path-dependence of the J-integral in incremental plasticity, GKSS Forschungszentrum, Geesthacht 1 (2001) 1–33.

[39] V. Kumar, M. German, C. F. Shih, Engineering approach for elastic-plastic fracture analysis, Tech. rep., General Electric Co. and Electric Power Research Institute (EPRI) (1981).

[40] M. Nevalainen, R. H. Dodds, Numerical investigation of 3-D constraint effects on brittle fracture in SE(B) and C(T) specimens, International Journal of Fracture 74 (2) (1996) 131–161. `doi:https://doi.org/10.1007/BF00036262`.

[41] R. Ainsworth, M. Gintalas, M. Sahu, J. Chattopadhyay, B. Dutta, Application of failure assessment diagram methods to cracked straight pipes and elbows, International Journal of Pressure Vessels and Piping 148 (2016) 26 – 35. `doi:https://doi.org/10.1016/j.ijpvp.2016.10.005`.
URL `http://www.sciencedirect.com/science/article/pii/S0308016116303660`

[42] K. Lu, T. Meshii, Three-dimensional T-stresses for three-point-bend specimens with large thickness variation, Engineering Fracture Mechanics 116 (2014) 197 – 203. `doi:https://doi.org/10.1016/j.engfracmech.2013.12.011`.
URL `http://www.sciencedirect.com/science/article/pii/S0013794413004050`

[43] Z. Liu, D. Yu, J. Tang, X. Chen, X. Wang, Stress intensity factor and T-stress solutions for three-dimensional clamped single edge notched tension (SENT) specimens, International Journal of Pressure Vessels and Piping 168 (2018) 11 – 23. `doi:https://doi.org/10.1016/j.ijpvp.2018.08.006`.
URL `http://www.sciencedirect.com/science/article/pii/S0308016118301650`

[44] K. Kodancha, S. Kudari, Variation of stress intensity factor and elastic T-stress along the crack-front in finite thickness plates, Frattura ed Integrità Strutturale 3 (8) (2009) 45–51.

[45] V. S. Barbosa, C. Ruggieri, Fracture toughness testing using non-standard bend specimens part ii: Experiments and evaluation of t0 reference temperature for a low alloy structural steel, Engineering Fracture Mechanics 195 (2018) 297 – 312. `doi:https://doi.org/10.1016/j.engfracmech.2018.03.028`.
URL `http://www.sciencedirect.com/science/article/pii/S0013794418300237`

[46] T. Meshii, Failure of the astm e 1921 master curve to characterize the fracture toughness temperature dependence of ferritic steel and successful application of the stress distribution t-scaling method, Theoretical and Applied Fracture Mechanics 100 (2019) 354 – 361. `doi:https://doi.org/10.1016/j.tafmec.2019.01.027`.
URL `http://www.sciencedirect.com/science/article/pii/S0167844218305962`

[47] S.-X. Wu, Y.-W. Mai, B. Cotterell, Plastic η-factor (η_{p}), International Journal of Fracture 45 (1) (1990) 1–18.

[48] R. Ainsworth, N. Odowd, Constraint in the failure assessment diagram approach for fracture assessment, ASME J Pres Ves Tech 117(3), 260-267`doi:https://doi.org/10.1115/1.2842121`.

[49] T.-L. Sham, The determination of the elastic T-term using higher order weight functions, International Journal of fracture 48 (2) (1991) 81–102.

[50] T. Fett, T-stresses in rectangular plates and circular disks, Engineering Fracture Mechanics 60 (5) (1998) 631 – 652. `doi:https://doi.org/10.1016/S0013-7944(98)00038-1`.
URL `http://www.sciencedirect.com/science/article/pii/S0013794498000381`

Appendix A Closed-form stress intensity factor, limit load and T-stress solutions

A.1 SENB specimen

The limit load, $\mathrm{P_L}$, for the SENB specimen (Fig. 1a) is [27]:

$$\mathrm{P_L} = \left(\frac{\mathrm{W^2 B}\sigma_\mathrm{y}}{\mathrm{H}}\right)\mathrm{f_L} \tag{A.1}$$

where W, B and H are the specimen width, thickness and span, respectively. With the von-Mises yield criterion, $\mathrm{f_L}$, for plane strain conditions is:

$$\mathrm{f_L} = \begin{cases} \frac{2}{\sqrt{3}}\left(1.12 + 1.13\alpha - 3.194\alpha^2\right)(1-\alpha)^2 & \text{for } 0 \leq \alpha \leq 0.18 \\ \frac{2.44}{\sqrt{3}}(1-\alpha)^2 & \text{for } 0.18 < \alpha < 1 \end{cases} \tag{A.2}$$

where α is the relative crack depth, a/W. The stress intensity factor for the opening mode is

[27]:

$$\mathrm{K_I} = \frac{3\mathrm{PH}}{2\mathrm{BW}^{1.5}}\mathrm{f}_\alpha \tag{A.3}$$

where P is applied load and the function f_α for H/W = 4 is:

$$\mathrm{f}_\alpha = \sqrt{\alpha}\frac{1.99 - \alpha(1 - \alpha)(2.15 - 3.93\alpha + 2.7\alpha^2)}{(1 + 2\alpha)(1 - \alpha)^{1.5}} \tag{A.4}$$

The plane strain value of β_T for H/W = 4, valid for $0 \le \alpha \le 0.8$, is [27]:

$$\beta_\mathrm{T} = -0.9893 + 4.8784(\alpha) - 9.6956(\alpha)^2 + 11.434(\alpha)^3 - 5.9061(\alpha)^4 \tag{A.5}$$

A.2 Pin-gripped SENT(P)

A general view of the single edge notched tension specimen is shown in Fig. 2a. This specimen may be subjected to clamped (Section A.3) or pin-gripped loading as illustrated by the finite element models in the deformed states in Figs 2b, 2c, respectively. Under pin-gripped loading conditions both ends of the specimen are subjected to an uniform stress distribution as shown in Fig. 2a. There is no constraint on rotation; the ends of the specimen are free to rotate. This is visible from the finite element model in Fig. 2c, where the ends of the specimen are no longer perpendicular to the load in the deformed state. The plane strain limit load for the SENT(P) specimen is [27]:

$$\mathrm{P_L} = \mathrm{WB}\sigma_\mathrm{y}\mathrm{f_L} \tag{A.6}$$

where

$$\mathrm{f_L} = \begin{cases} (\gamma/1.702)\left(1-\alpha-1.232\alpha^2+\alpha^3\right) & \text{for } 0 \le \alpha \le 0.545 \\ \gamma\left[\sqrt{(0.794-(1-\alpha))^2+0.5876\,(1-\alpha)^2}-(0.794-(1-\alpha))\right] & \text{for } 0.545 < \alpha < 1 \end{cases} \tag{A.7}$$

with $\gamma = 3.404/\sqrt{3}$

For the normalised length of the specimen given by H/W=12 and for $0 < \alpha < 0.8$, the normalised constraint parameter is [27]:

$$\beta_\mathrm{T} = -0.5889 - 0.0128(\alpha) + 0.5512(\alpha)^2 + 4.651(\alpha)^3 - 4.6703(\alpha)^4 \tag{A.8}$$

The stress intensity factor solution is [15]:

$$\mathrm{K_I} = \sigma\sqrt{\pi \mathrm{a}}\mathrm{f}_\alpha \tag{A.9}$$

with the correction function given by:

$$\mathrm{f}_\alpha = \sqrt{\frac{2\mathrm{W}}{\pi\alpha}\tan(0.5\pi \mathrm{a})}\frac{0.752+2.02(\alpha)+0.37\,(1-\sin(0.5\pi\alpha))^3}{\cos(0.5\pi\alpha)} \tag{A.10}$$

A.3 Clamped gripped SENT(C)

Under clamped-grip loading conditions, the ends of the specimen are subjected to uniform displacement. Due to the clamping, there is no rotation allowed at the specimen ends. Therefore, both ends remain perpendicular to the load vector. This can be seen from the finite element model in Fig. 2b. The limit load for the SENT(C) specimen under plane strain conditions is calculated from Eq. (A.6), but using the following expression for $\mathrm{f_L}$ [27]:

$$\mathrm{f_L} = \frac{\gamma}{1.702}(1 - \alpha) \quad \text{for } 0 \leq \alpha < 1 \tag{A.11}$$

For H/W=5 and for $0 < \alpha < 0.55$ [27]:

$$\beta_{\mathrm{T}} = -0.5889 + 0.1022(\alpha) + 1.588(\alpha)^2 - 2.7591(\alpha)^3 + 1.4230(\alpha)^4 \tag{A.12}$$

The stress intensity factor is calculated from Eq. (A.9) using values of f_α from Table 9.

Table 9: Normalised stress intensity factor for H/W=5 for SENT(C) [33]

α	0.0	0.1	0.15	0.2	0.25	0.3	0.35	0.4	0.45
f_α	0.122	1.159	1.205	1.263	1.332	1.412	1.501	1.599	1.706
α	0.5	0.55	0.6	0.65	0.7	0.75	0.8	0.85	0.9
f_α	1.823	1.949	2.085	2.229	2.384	2.554	2.748	2.992	3.372

A.4 Pipe under bending with a through-wall circumferential crack (TWC)

The pipe geometry is shown in Fig. 3. The limit bending moment is [27]:

$$\mathrm{M_L} = 4\mathrm{R_m^2}\mathrm{t}\sigma_{\mathrm{y}}\left[\cos(\theta/2) - (1/2)\sin(\theta)\right]\left[1 + (1/12)(\mathrm{t}/\mathrm{R_m})^2\right] \tag{A.13}$$

where $\mathrm{R_m}$ is the mean radius, t is the wall thickness and 2θ is the circumferential angle of the defect.

The corresponding stress intensity factor is:

$$\mathrm{K_I} = \sigma_\mathrm{b}\sqrt{\pi \mathrm{a}}\mathrm{f}_\alpha \tag{A.14}$$

where the bending stress, $_\mathrm{b}$, is related to the applied moment, M, by:

$$\sigma_\mathrm{b} = \mathrm{M}/\left(\pi \mathrm{t} \mathrm{R}_\mathrm{m}^2\right) \tag{A.15}$$

The stress intensity factor function, f_α, and the normalised constraint parameter β_T are obtained from the same form of an equation:

$$\mathrm{f}_\alpha, \beta_\mathrm{T} = (\mathrm{f}, \mathrm{b})_0 + (\mathrm{R_m/t})(\mathrm{x}_1) + (\mathrm{R_m/t})^2(\mathrm{x}_2) + (\theta/\pi)(\mathrm{x}_3) \tag{A.16}$$

where

$$\mathrm{x}_1 = (\mathrm{f}, \mathrm{b})_1 + (\mathrm{f}, \mathrm{b})_2(\theta/\pi) + (\mathrm{f}, \mathrm{b})_3(\theta/\pi)^2 + (\mathrm{f}, \mathrm{b})_4(\theta/\pi)^3 + (\mathrm{f}, \mathrm{b})_5(\theta/\pi)^4 \tag{A.17}$$

$$\mathrm{x}_2 = (\mathrm{f}, \mathrm{b})_6 + (\mathrm{f}, \mathrm{b})_7(\theta/\pi) + (\mathrm{f}, \mathrm{b})_8(\theta/\pi)^2 + (\mathrm{f}, \mathrm{b})_9(\theta/\pi)^3 \tag{A.18}$$

$$\mathrm{x}_3 = (\mathrm{f}, \mathrm{b})_{10} + (\mathrm{f}, \mathrm{b})_{11}(\theta/\pi) + (\mathrm{f}, \mathrm{b})_{12}(\theta/\pi)^2 + (\mathrm{f}, \mathrm{b})_{13}(\theta/\pi)^3 + (\mathrm{f}, \mathrm{b})_{14}(\theta/\pi)^4 \tag{A.19}$$

The coefficients $\mathrm{f}_1 - \mathrm{f}_{14}$ and $\mathrm{b}_1 - \mathrm{b}_{14}$ can be found in [34].

A.5 Pipe with a fully-circumferential internal crack (FCC) in tension

A pipe with a fully circumferential internal crack subjected to end loads is shown in Fig. 4a. The external and internal radii are denoted $\mathrm{R_e}$ and $\mathrm{R_i}$, respectively. Crack length is a and wall thickness is W (Fig. 4b).

The limit load for internal cracks is [27]:

$$\mathrm{P_L} = \mathrm{f_L} 2\pi \mathrm{R_m} \mathrm{W} \sigma_\mathrm{y} \tag{A.20}$$

with the function $\mathrm{f_L}$ given by:

$$\mathrm{f_L} = \begin{cases} \frac{(1+\eta_\mathrm{i})^2-(1+\alpha\eta_\mathrm{i})^2}{(1+\eta_\mathrm{i})^2-1}\left(\sqrt{1-\mathrm{p_i^2}}+\mathrm{A_i p_i}\right) & \text{for } \alpha \leq (\mathrm{a_0})_\mathrm{i} \\ \frac{(1+\eta_\mathrm{i})^2-(1+\alpha\eta_\mathrm{i})^2}{(1+\eta_\mathrm{i})^2-1}\sqrt{1-\mathrm{A_i^2}} & \text{for } \alpha > (\mathrm{a_0})_\mathrm{i} \end{cases} \tag{A.21}$$

where α=a/W; $\eta_\mathrm{i} = \mathrm{W/R_i}$. The parameters $\mathrm{p_i}$, $(\mathrm{a_0})_\mathrm{i}$ and $\mathrm{A_i}$ are calculated from:

$$\mathrm{p_i} = \frac{\alpha\eta_\mathrm{i} - 0.684\,(\alpha\eta_\mathrm{i})^2 + 0.2475\,(\alpha\eta_\mathrm{i})^3}{\frac{2}{\sqrt{3}}\ln\left(\frac{1+\eta_\mathrm{i}}{1+\alpha\eta_\mathrm{i}}\right)} \text{for } \alpha\eta_\mathrm{i} \leq 1 \tag{A.22}$$

$$(\alpha_0)_\mathrm{i} = 0.366 - 0.1994\eta_\mathrm{i} + 0.0504\eta_\mathrm{i}^2 - 0.0055\eta_\mathrm{i}^3 \text{ for } \eta_\mathrm{i} \leq 3 \tag{A.23}$$

$$\mathrm{A_i} = \frac{2}{\sqrt{3}} \frac{\ln\left(\frac{1+\eta_\mathrm{i}}{1+\alpha\eta_\mathrm{i}}\right)}{\left(\frac{1+\eta_\mathrm{i}}{1+\alpha\eta_\mathrm{i}}\right)^2 - 1} \tag{A.24}$$

The stress intensity factor is defined by:

$$\mathrm{K_I} = \sigma_\mathrm{m}\sqrt{\pi \mathrm{a}}\mathrm{f}_\alpha \tag{A.25}$$

where values for the coefficient f_α are given in Table 10 and σ_m is longitudinal stress in the wall due to the axial load P:

$$\sigma_\mathrm{m} = \frac{\mathrm{P}}{\pi\left(\mathrm{R_e^2} - \mathrm{R_i^2}\right)} \tag{A.26}$$

Table 10: Correction coefficients of stress intensity factor for FCC pipe with $\mathrm{W/R_i}$=0.2 [29]

a/t	0.0	0.2	0.4	0.6	0.8
f_α	1.122	1.215	1.446	1.804	2.280

The normalised constraint parameter for $\mathrm{R_i/W}$=5 is [27]:

$$\beta_\mathrm{T} = -0.51 - 0.4074(\alpha) + 4.0608(\alpha)^2 - 13.768(\alpha)^3 + 27.014(\alpha)^4 - 28.024(\alpha)^5 + 11.33(\alpha)^6 \tag{A.27}$$